ACS OMEGA

Open Access

http://pubs.acs.org/journal/acsodf

Article

Coexistence of WORM and RRAM Resistive Switching in Coumarin Derivatives: A Comprehensive Performance Analysis

Rahul Deb, Hritinava Banik, Utpal Chandra De, Debajyoti Bhattacharjee, Khuloud A. Alibrahim, Abdullah N. Alodhayb, and Syed Arshad Hussain*

Cite This: *ACS Omega* 2025, 10, 11091−11107

Read Online

ACCESS | Metrics & More | Article Recommendations | Supporting Information

ABSTRACT: Over the past few years, organic small molecules (OSM) having a π-conjugated heteroatomic aromatic backbone along with terminal donor−acceptor (D-A) groups have emerged as one of the most promising materials for organic resistive switching (ORS) devices. In this research, the resistive switching (RS) properties of two rationally synthesized coumarin derivatives, 7-(2-(benzylamino)ethoxy)-4-methyl-2H-chromen-2-one (CAMN1) and 7-(2-(4-methoxyphenylamino)ethoxy)-4-methyl-2H-chromen-2-one (CAMN2), have been exhaustively studied. The CAMN1-based ORS device exhibited WORM RS behavior with an excellent device yield of 97.22%, while the CAMN2-based device showed both WORM as well as RRAM RS behavior depending on the compliance current (CC) with a perfect device yield of 100%. Both devices exhibited superior read endurance on the order of 10^4 as well as a retention time of at least 3×10^4 s with a very good memory window of the order of 10^4 or more. Moreover, both devices exhibited superior long-term physical and thermal stability. The cyclability of the CAMN2-based device in the RRAM mode of operation was found to be 116 cycles. DFT-based calculations as well as absorption spectroscopic studies reveal the role of the intra/intermolecular charge transfer (CT) in the RS behavior of both the devices. Moreover, the presence of the methoxy (−OCH$_3$) group in the CAMN2 molecule has been identified as the key reason behind the observed difference in the RS behaviors of the two molecules.

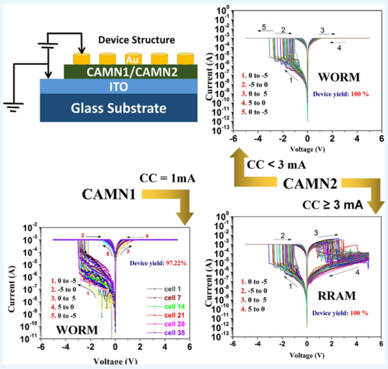

I. INTRODUCTION

The current pace of development in advanced data driven technologies like the Internet of things (IOT), artificial intelligence (AI), machine learning (ML), Big Data etc. creates an ever increasing demand for ultrahigh density data storage as well as high speed computing devices.[1] The conventional silicon-based memory and computing devices are soon to become incompatible with this ever increasing demand due to numerous perceptible drawbacks of these devices, such as low data fidelity, low speed, heat death, high manufacturing expenses, high power consumption, lack of down scalability as well as low packing density.[2−4] On the other hand, over the past decade, significant progress has been made in organic resistive switching (ORS) technology making it a promising candidate for post-Moore electronics.[2,4−10] Distinctive advantages, such as faster switching speed, lower power consumption, higher packing density, higher data fidelity, ease of processing, low-cost fabrication, etc. make the ORS devices one of the prime candidates for next generation information storage systems.[4,11−13] Moreover, these devices can also realize in-memory computation providing a feasible solution to the von-Neumann bottleneck problem.[14]

In general, ORS devices, having a simple 2D metal−insulator−metal (MIM) structure, utilize the various stable resistance states of the active organic layer to store binary or even multiple bit data.[11,15] For an organic material-based device with two stable resistance states, one state can be considered as the "OFF" state (binary "0") and the other state as the "ON" state (binary "1").[11,12] The resistance states of such devices can be programmed by applying suitable voltage biases either from the "OFF" to the "ON" state or from the "ON" to the "OFF" state corresponding to the SET and RESET operations, respectively, in digital electronics.[8,15] The OSM devices in which both SET and RESET operations can be performed are ideal for resistive-random-access-memory (RRAM) applications where write-read-erase-read-rewrite operations can be realized using appropriate bias voltage.[13,16] Such devices have widespread applications in rewritable data storage as well as computation technologies.[17] On the other hand, in some cases when an ORS device is SET to its "ON" state, it cannot be RESET to its original (OFF) state. ORS devices with such switching behavior are ideal for write-once-

Received: November 1, 2024
Revised: February 27, 2025
Accepted: March 4, 2025
Published: March 13, 2025

Scheme 1. Synthesis of C-7(O) Modified 4-Methyl Coumarin Derivatives CAMN1 and CAMN2[a]

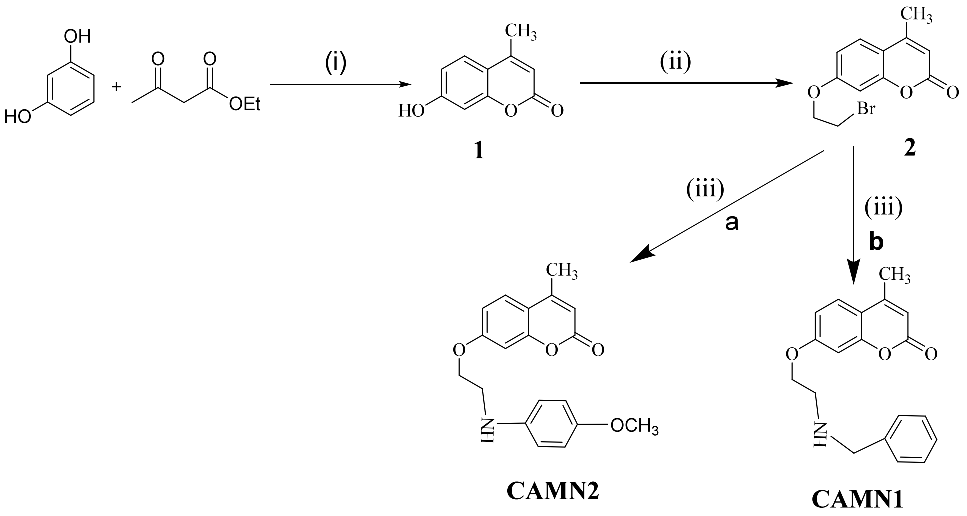

[a]Reagents and conditions: (i) Conc. H_2SO_4, 0 °C, 24 h; (ii) 1,2-dibromoethane, K_2CO_3, reflux, 60-70 °C, 12–20 h; (iii) a. $C_6H_5CH_2$-NH_2, b. *p*-MeO-$C_6H_4NH_2$ in presence of, 80–100 °C, 12–18 h.

read-many (WORM) applications where once the data is written, it cannot be erased but read multiple times.[15,18,19]

In recent times, various organic and organo-composite materials, including organic small molecules (OSM), polymers with π-conjugated backbone, organic polymer blends, biopolymers, metalopolymers, organo-metallic complexes, organic–inorganic-hybrid perovskites etc., have emerged as promising materials for ORS active layers with apt results.[2,5−13,16,18,20−31] In this regard, OSM attract the most attention due to their versatile molecular organization and superior reproducibility.[7−9,11,21,23,28] OSM having a π-conjugated heteroatomic aromatic backbone along with terminal donor–acceptor (D-A) groups have been found to exhibit excellent nonvolatile memory behavior.[11,13,28,32] For example, WORM type ORS memory devices have been recently developed by Nagarajan et al. based on a series of synthesized OSM with A-π-D-π–A- and D-π-D-π-D structures comprising a bis(triphenylamine)-based molecular backbone and ethynyl-linked electron donor/acceptor groups.[28] Li et al. designed a series of mono-, di-, tribranched quinoxaline derivatives-based ORS memory devices with binary as well as ternary WORM type switching behavior.[32] In most cases, the resistive switching (RS) behavior of these OSM-based devices can be attributed to the voltage bias induced intra/intermolecular charge transfer (CT) from the donor part of the OSM to the acceptor part of the same molecule or to the acceptor part of the neighboring molecule.[9,11,23,28] Moreover, the donor/acceptor moieties may act as charge traps within the active layer promoting the overall memory performance of the devices.[11,28] In spite of having several such advantageous properties, most OSM-based ORS devices deliver underwhelming performance in terms of device yield, long-term physical stability as well as thermal stability.[8,11,13] In order to address these issues, it becomes important to develop a new class of OSM with robust RS behavior. In this regard, coumarin derivatives may serve as ideal candidates for ORS devices. Coumarin or 2H-chromen-2-one belongs to the benzopyrone family and is one of the most versatile and extensively researched molecular scaffolds.[33] It consists of a an α-pyrone ring fused with a benzene nucleus.[34,35] Coumarin was first reported by A. Vogel in 1820 and has been reported in various plant species thenceforth.[36] Due to its unique molecular structure, it exhibits widespread inter/intramolecular interactions including hydrophobic, hydrogen bonds and electrostatics interactions with interesting optoelectronic properties.[37] Coumarin derivatives are reported to be good electron donors having high π-conjugation and relatively low oxidation potentials due to which coumarin and its derivatives have attracted widespread research interest in organic semiconducting materials applications such as, solar energy collectors, potential organic light-emitting diodes as well as organic resistive switching (ORS) devices.[38−40] Moreover, it is possible to easily modulate the optoelectronic and resistive switching (RS) behavior of coumarin derivatives through chemical modification.[37] Paul et al. explored the RRAM and threshold RS behavior of the some 7-Alkoxy-appended coumarin derivatives with D-π-A structures by varying the donor and acceptor moieties.[41] However, the work lacks a detailed evaluation of the various performance parameters. Moreover, we have recently demonstrated WORM type resistive switching in a coumarin derivative, namely, 7-hydroxy-N-octadecyl coumarin-3-carboxamide (7HNO3C) with device structure Al/7HNO3C/ITO.[11] The performance of the device was enhanced across several memory parameters (device yield, retention time, memory window, and read endurance) by incorporating ZnO nanoparticles within the active layer of the device. In light of the above discussion, it will be an interesting endeavor to identify novel coumarin derivatives that may serve as active layer materials in ORS devices with reliable performance. Moreover, it will also be interesting to see how structural modifications in such coumarin derivatives affect the performance of such devices across various memory parameters.

In the present work, the ORS behavior of two rationally synthesized coumarin derivatives, namely, 7-(2-(benzylamino)-ethoxy)-4-methyl-2H-chromen-2-one (CAMN1) and 7-(2-(4-methoxyphenylamino)ethoxy)-4-methyl-2H-chromen-2-one (CAMN2) has been thoroughly investigated. It has been found that the presence of the electron-rich (electron-donating) -OCH_3 group plays a crucial role in determining the RS behavior (WORM or RRAM) of the coumarin derivatives. The

-OCH_3 containing molecule CAMN2 exhibited both WORM as well as RRAM RS behavior depending on compliance current (CC). On the other hand, the CAMN1 (excluding the -OCH_3 group) molecule exhibited only WORM type RS behavior independent of CC. Moreover, in order to evaluate the memory permanence of these devices, various memory parameters are thoroughly investigated. It has been found that both devices exhibit very high device yield, memory window, excellent read endurance, data retention characteristic as well as superior physical and thermal stability.

II. EXPERIMENTAL SECTION

Materials. Resorcinol (purity, ≥ 99.0%), ethyl acetoacetate (purity, 99%), benzylamine (purity, 99%), *p*-methoxyaniline (purity, 99%), anhydrous K_2CO_3 (purity, 99%), ethyl acetate (purity, 99.8%), and petroleum ether (purity, ≥ 90%) have been procured from Sigma-Aldrich and used without further purification. ITO-coated glass substrates of sheet resistance 70−100 Ω/sq was purchased from Sigma-Aldrich. Silica gel plates (60 F254; Merck) were used for monitoring chemical reactions. Spectroscopic grade chloroform (99.9%, SRL, India) and dry DMF (99.8%, ACS reagent) were used as solvents as per requirement.

Synthesis of Compounds. Compound 1 and 2 were prepared according to Pechmann reaction procedure using commercially available (Sigma-Aldrich) resorcinol and ethyl acetoacetate.[36] It was then converted to the intermediate 2 according to the literature method.[42] Subsequently, intermediate 2 was reacted separately with benzylamine and *p*-methoxyaniline at 70 °C in the presence of anhydrous K_2CO_3 in dry DMF (Scheme 1) to afford CAMN-1 and CAMN-2 respectively. Reaction was constantly monitored by thin-layer chromatography (TLC) on silica gel plates (60 F254; Merck), visualized with iodine vapors and ultraviolet light. The reaction products were purified by column chromatography and Flash chromatography (Isolera Prime, Biotage, Sweden) eluting with the mixtures of ethyl acetate and petroleum ether. NMR spectra of CAMN1and CAMN2 have been shown in Figures S1 and S2 of Supporting Information (SI). Chemical structures of the coumarin derivatives (CAMN1 and CAMN2) are shown in Figure 1a,b, respectively.

7-(2-(Benzylamino)ethoxy)-4-methyl-2H-chromen-2-one (CAMN1). White solid, 75% yield; mp 152 °C; IR (KBr) ν 3446 (N−H), 2925 (C−H), 1713 (C═O), 1622 (C═C) cm^{-1}; 1H NMR (400 MHz, CDCl3) δ (ppm): 2.41 (s, 3H), 3.09 (t, 2H, J = 3.2 Hz), 3.68 (s, 1H), 3.91 (s, 2H), 4.16 (t, 2H, J = 3.2 Hz), 6.15 (s, 1H), 6.83 (s, 1H), 6.88 (d, 1H, J = 5.6 Hz), 7.32 (m, 2H), 7.36 (m, 3H), 7.50 (d, 1H, J = 5.6 Hz); 13C NMR (100 MHz, CDCl3) δ (ppm): 161.86, 161.30, 155.23, 152.53, 139.72, 128.53, 128.28, 128.21, 127.20, 125.54, 113.73, 112.50, 112.05, 101.55, 68.05, 53.79, 47.79. GCMS (*m*/*z*): calcd for C19H19NO3 309.36, found 309.40.

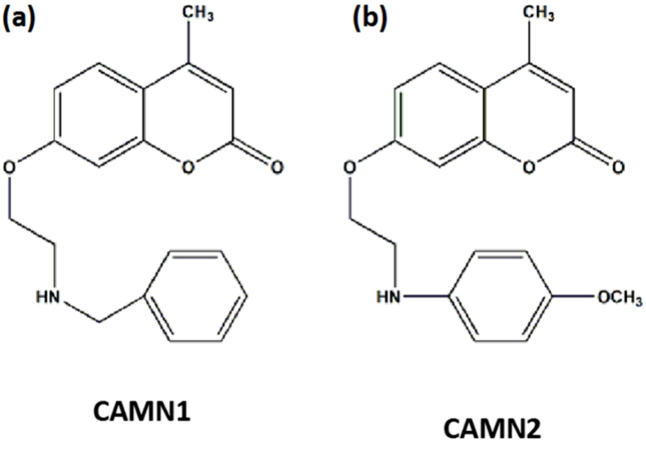

Figure 1. Chemical structures of CAMN1 (a) and CAMN2 (b).

7-(2-(4-Methoxyphenylamino)ethoxy)-4-methyl-2H-chromen-2-one (CAMN2). Gray solid. 60% yield; mp 146 °C; IR (KBr) ν 3380 (N−H), 2933 (C−H), 1714 (C═O), 1615 (C═C) cm-1; 1H NMR (400 MHz, CDCl3) δ (ppm): 2.40 (s, 3H), 3.55(t, 2H, J = 3.2 Hz), 3.77 (s, 3H), 4.22 (t, 2H, J = 3.2 Hz), 6.15 (s, 1H), 6.69 (d, 2H, J = 5.6 Hz), 6.83 (d, 3H, J = 6.4 Hz), 6.90 (d, 1H, J = 6 Hz), 7.51 (d, 1H, J = 6 Hz); 13C NMR (100 MHz, CDCl3) δ (ppm): 161.69, 161.20, 155.22, 152.65, 152.48, 141.71, 125.63, 114.99, 114.72, 113.88, 112.44, 112.16, 101.62, 67.20, 55.80, 44.14, 18.67. GCMS (*m*/*z*): calcd for C19H19NO4 325.36, found 325.40.

Device Fabrication. In order to assess the I−V characteristics of the synthesized molecules CAMN1 and CAMN2, two devices, namely, device D_1 and device D_2, having device structures Au/CAMN1/ITO and Au/CAMN2/ITO, respectively, have been fabricated. For the fabrication of the devices, working solutions of CAMN1 (0.5 mg/mL) and CAMN2 (0.5 mg/mL) have been prepared with chloroform as solvent. Here, CAMN1 and CAMN2 act as the active layers in devices D_1 and D_2, respectively. The active layers of the devices were deposited onto ITO-coated glass substrates by a spin coating method using a commercially available spin coating instrument (EZspin-SD, Apex Instruments Co, India). In order to do that, the prepared solutions of the active materials were spread onto ITO-coated glass substrate, dropwise, while spinning the substrate for 60 s for each drop at an optimized rotation rate of 900 rpm. Subsequently, the spin-coated films were allowed to dry in a vacuum chamber for 10 h prior to further processing. Afterward, arrays (6 × 6) of 36 Au electrodes, having an active area of 500 μm^2, were deposited onto the active layers of both devices by vacuum deposition method (vacuum coating unit Model 12A4D, Hind High Vacuum Co. (P) Ltd.). In both devices, Au and ITO act as the top and the bottom electrodes, respectively. Subsequently, the fabricated devices were kept in a vacuum chamber prior to electrical measurements. Schematic of the device structures of both devices as well as their optical images are shown in Figure 2.

Measurements and General Methods. Electrical characterization of the fabricated devices has been carried out in ambient conditions using a Keithley sourcemeter (Model No. 2614B) and probe station (Everbeing C2). DC staircase sweeps of optimized magnitude and direction were employed in order to obtain the optimum I−V response of the devices. While the I−V characteristics were recorded, the step voltage was set at 0.05 V per step. A commercially available field-emission scanning electron microscope (FESEM) (model no. Sigma 300, Zeiss Pvt Ltd.), operating at an accelerating potential of 5KV, has been utilized in order to visualize the surface morphology of the active layers of both devices. A commercially available absorption spectrophotometer (Shimadzu, UV-1800) was used to record the UV−vis absorption spectra of the synthesized compounds (CAMN1 and CAMN2). The progress of the reactions was constantly monitored by thin-layer chromatography (TLC) on silica gel plates (60 F254; Merck) visualized with iodine vapors and

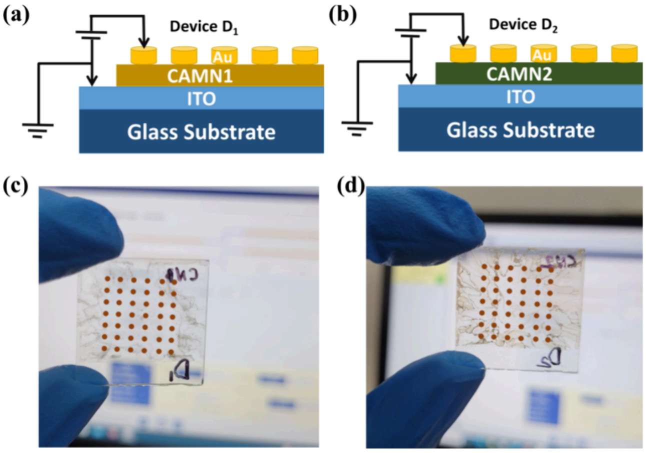

Figure 2. (a) Schematic diagram of device D_1. (b) Schematic diagram of device D_2. (c) Optical image of device D_1. (d) Optical image of device D_2.

ultraviolet light. Commercially available electrochemical workstation (Corr. Test; Model No.: CS350) was used to perform the cyclic voltammetry (CV) analysis of the compounds. Density functional theory (DFT) modeling has been performed employing GAUSSIAN-16 software applying the B3LYP functional at the 6-31g(d) level of theory.

III. RESULTS AND DISCUSSION

Morphological Characterization. Scanning electron micrographs were obtained by using FESEM in order to investigate the surface morphologies of the active layers of the devices. Figure 3a,3b depict the surface morphologies of spin-coated CAMN1 and CAMN2 films, respectively. As observed from the figures, compound CAMN1 forms a thread like aggregation (Figure 3a), whereas compound CAMN2 forms spherical aggregation (Figure 3b) in spin-coated thin films. Both compounds show well connected morphological structures at the nanoscale which may play a crucial role in providing efficient pathways for the charge carriers to migrate within the active layers of both devices.[28,43] Electrical characterization revealed that the observed differences in the nature of aggregations play a prominent role in charge carrier migration as well as in inter/intramolecular charge transfer (CT) complex formation.[23,28] This has been explored in detail in a later section of the manuscript. Figure 3c,d represent the cross-sectional FESEM images of device D_1 and D_2, respectively. The cross-sectional images reveal the formation

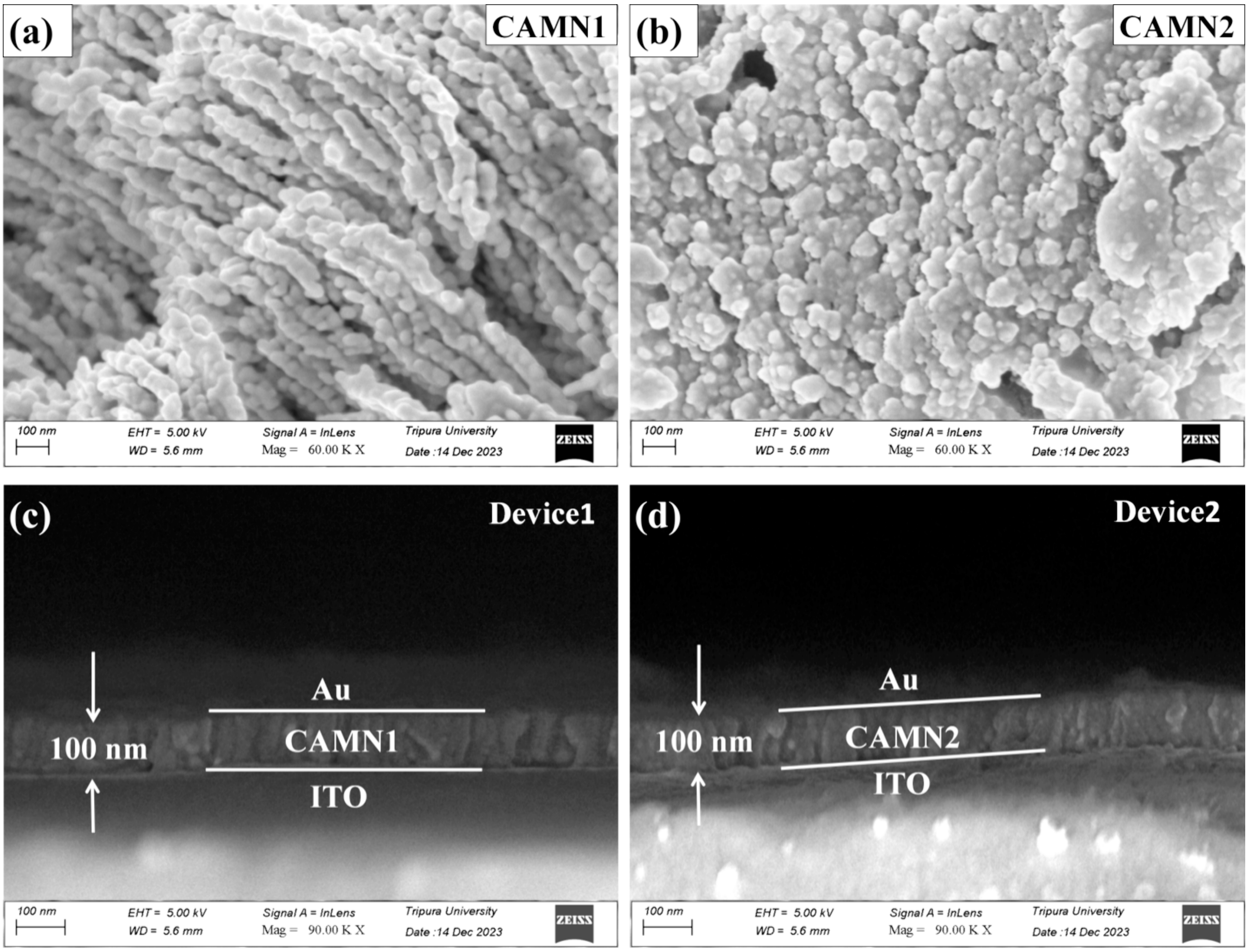

Figure 3. (a) FESEM image of a spin-coated CAMN1 film. (b) FESEM image of a spin-coated CAMN2 film. (c) Cross-sectional FESEM images of device D_1. (d) Cross-sectional FESEM images of device D_2.

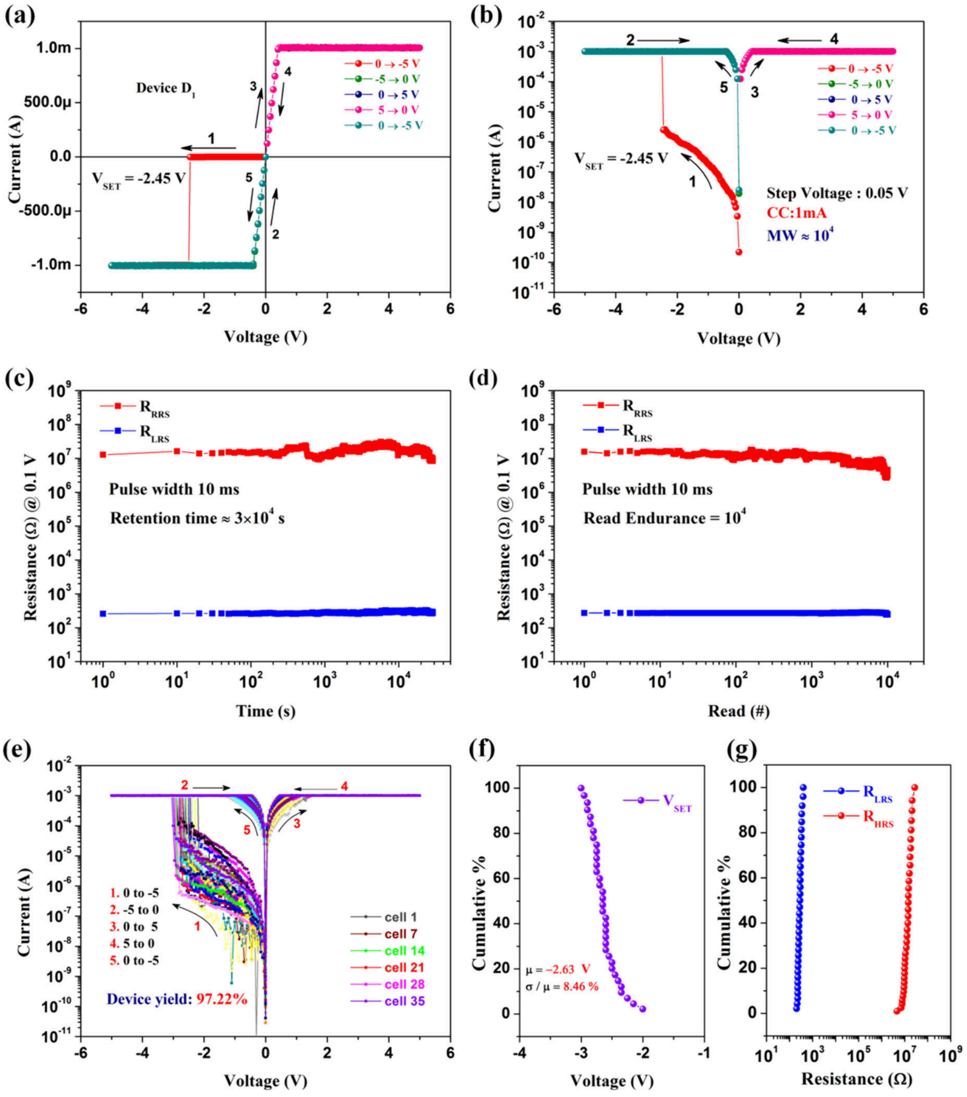

Figure 4. (a,b) I−V curves of device D_1 on the linear scale and semi logarithmic scale, respectively. (c) Data retention characteristics of device D_1. (d) Read endurance of device D_1. (e) I−V curves of the 35 memory cells showing reliable WORM type resistive switching in device D_1. (f) Cumulative probability of V_{SET} of 35 cells. (g) Cumulative probability of R_{LRS} and R_{HRS}.

of almost uniform active layers in devices D_1 and D_2. The thickness of the active layers in both devices is found to be approximately 100 nm. Moreover, the Au top electrode and the ITO bottom electrode are also clearly distinguishable in the cross-sectional images (Figure 3c,d).

Electrical Characterization. Figures 4a and 3b represent the I−V characteristics of device D_1, having CAMN1 as the active layer, in linear scale and semi logarithmic scale, respectively. The I−V response was recorded by applying DC staircase sweeps while keeping the compliance current (CC) set at an optimized value of 1 mA to prevent dielectric breakdown of the device active layer.[44] The sweep voltage range and sequence are included in the figures (Figure 4a,b). On application of the first voltage scan (0 V to −5 V), the device was found to be at the high resistance state (HRS) or "OFF state" initially. However, with the increase in the applied bias voltage, the device undergoes a sharp transition from the HRS to the low resistance state (LRS) or "ON state" at a threshold voltage of −2.45 V. This transition from HRS to LRS is known as the SET process or "data writing" process and the threshold voltage is known as the set voltage (V_{SET}).[13,15] Interestingly, on application of the subsequent voltage sweeps (−5 V → 0 V → 5 V → 0 V → 5 V), the device did not return to the HRS irrespective of the sweep direction and polarity. Moreover, the device maintained the LRS even when the external power was removed. Clearly, the device D_1 shows WORM type resistive switching (RS) behavior.[8,15] In such devices, once information is written, it cannot be erased or modified afterward. However, the stored information can be read multiple times by applying suitable read voltage pulses. RS devices with such behavior are ideal for all kinds of practical applications where permanent storage of data is necessary including archival storage, secure databases as well as secure communication.[8,11,15,18,35] The memory window of the device is found to be of the order of 10^4 at a data read out voltage of 0.1 V. Such a high memory window is desirable in RS devices as it minimizes the data read out error.[45]

In order to investigate the effects of higher CC in the observed RS behavior of D_1, the CC value was gradually raised from 1 mA up to 50 mA. It was observed that once the device was switched to the LRS, it maintained that state even when the value of CC was increased up to 50 mA (Figure S3 of the

Table 1. Cycle to Cycle Statistical Variation of the Various Memory Parameters of Device D_2 in RRAM Mode

performance parameter	range min	range max	mean	relative deviation
V_{SET}	−1 V	−2.7 V	−1.54 V	25.01%
V_{RESET}	0.9 V	2.75 V	1.79 V	20.08%
I_{SET}	1.40×10^{-7} A	2.7×20^{-5} A	2.4×10^{-6} A	149.37%
I_{RESET}	0.57×10^{-3} A	4.36×10^{-3} A	2.26×10^{-3} A	31.81%
R_{HRS}	4.72×10^{6} Ω	8.61×10^{7} Ω	2.39×10^{7} Ω	57.85%
R_{LRS}	390.54 Ω	1061.75 Ω	652.61 Ω	22.23%

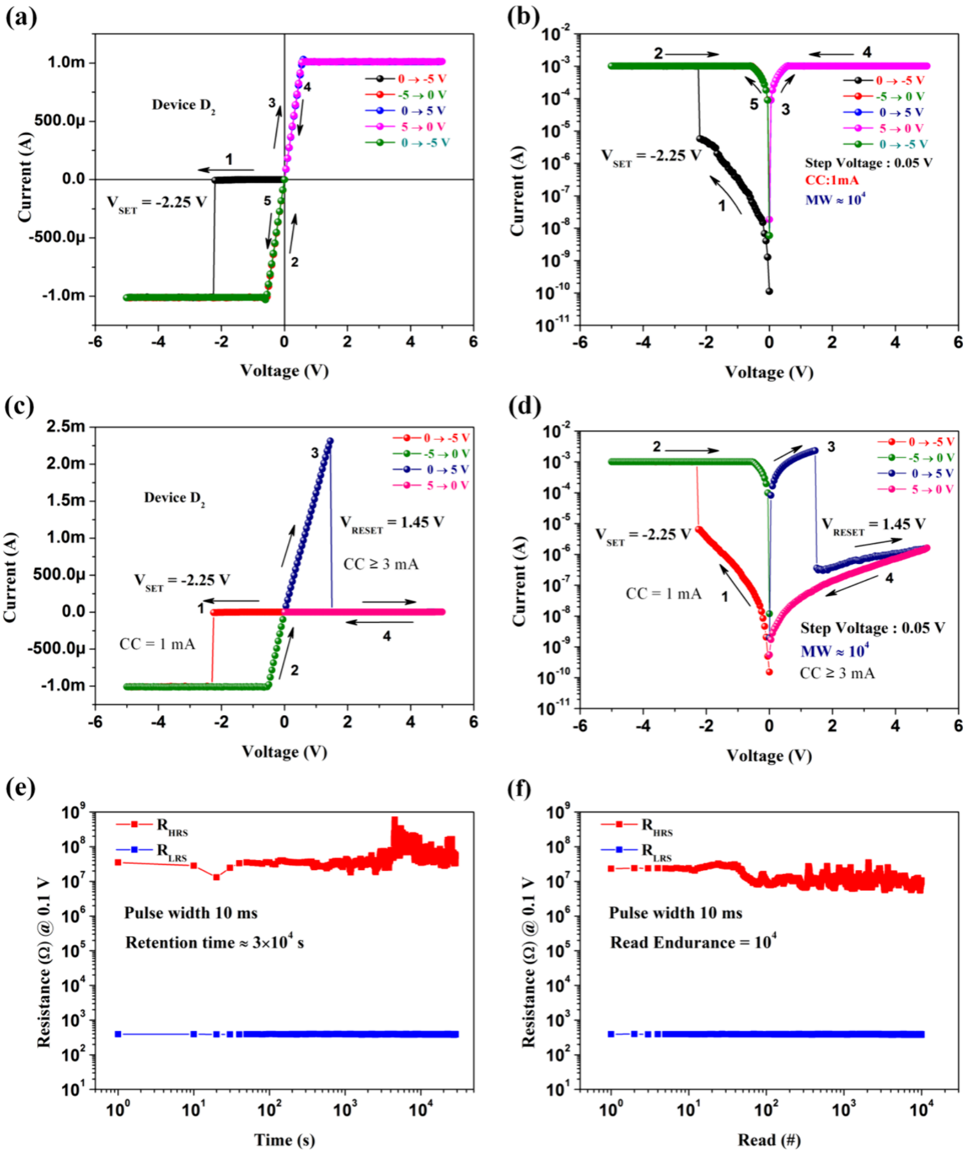

Figure 5. (a,b) I−V curves of device D_2 on the linear scale and semi logarithmic scale, respectively, showing WORM RS when CC is fixed at 1 mA in both polarities. (c,d) I−V curves of device D_2 on the linear scale and semi logarithmic scale, respectively, showing RRAM RS when CC inset at 1 mA in negative polarity and 50 mA in positive polarity.(e) Data retention characteristics of device D_2. (f) Read endurance of the device D_2.

SI). For a CC value higher than 50 mA, the active layer of the device got permanently damaged due to Joule's heating.[11] For further characterization of the device, the CC value was maintained at 1 mA. Low read voltage as well as low CC values are always desirable in RS devices as it is related to low power consumption requirement. Moreover, high CC may also significantly alter the read endurance and data retention characteristics of the device.[45]

In order to assess the data retention characteristics of the device D_1, the values of HRS and LRS resistances (R_{HRS} and R_{LRS}, respectively) have been measured by applying read voltage pulses of amplitude 0.1 V and pulse with 10 ms continuously, at an interval of 10 s for 3×10^4 s[11]. The measured resistance values are plotted against time, as shown in Figure 4c. As observed from the Figure 4c, the values of R_{HRS} an R_{LRS} show negligible variation for the entire duration

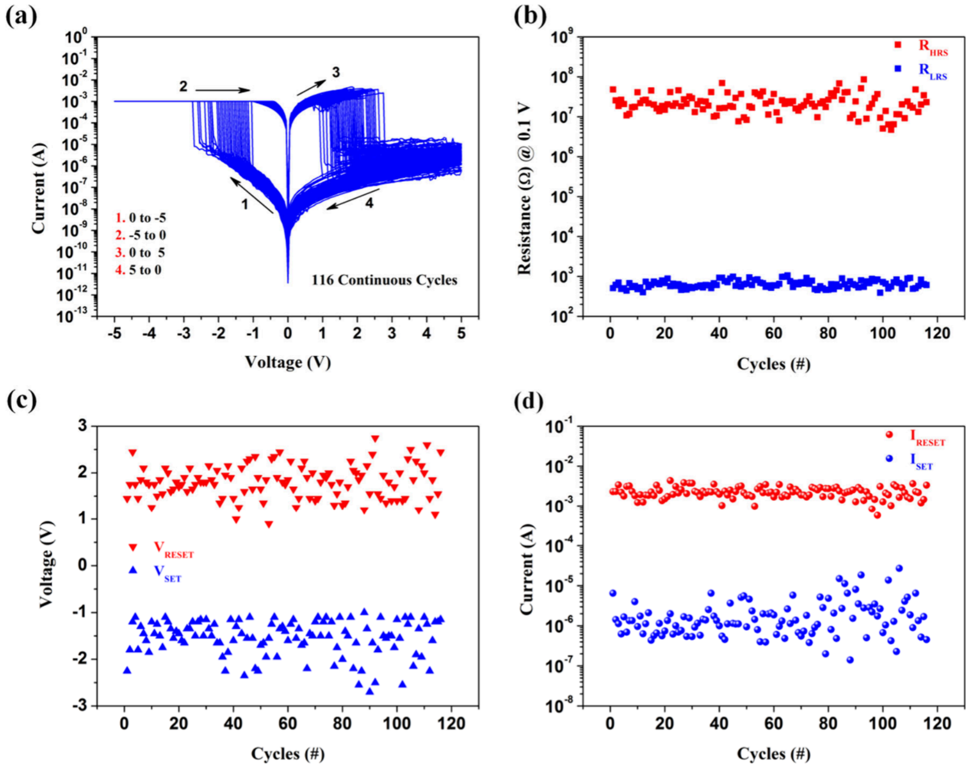

Figure 6. (a) I−V response of D_2 for 116 continuous switching cycles. (b) Cycle to cycle variation of R_{HRS} and R_{LRS}. (c) Cycle to cycle variation of V_{SET} and V_{RESET}. (d) Cycle to cycle variation of I_{SET} and I_{RESET}.

of measurement which indicate that the device D_1 can retain the stored data for at least 3×10^4 s. Moreover, the read endurance of the device has also been evaluated by measuring the values of R_{HRS} and R_{LRS} by applying read voltage pulses of amplitude 0.1 V and pulse width 10 ms for 10^4 times at an interval of 10 ms[11]. The measured values of R_{HRS} and R_{LRS} are plotted against pulse number as depicted by Figure 4d. The values of R_{HRS} and R_{LRS} remains stable for at least 10^4 reading cycles as evident from the Figure 4d. This suggests that once the data are written in the memory device, they can be read at least 10^4 times without any read error.

From the application point of view, it is important to ensure that the desired memory behavior is observed in a statistically significant number of devices with an acceptable device yield.[46] This gives an idea about device reproducibility with almost negligible error, which is very important for large-scale production for future applications. In order to assess the reproducibility of the device as well as to investigate the device-to-device (D2D) variability of the various switching parameters, we have fabricated 36 memory units in a 6 × 6 array having device structure identical to that of device D_1. The I−V measurements of these memory cells indicate that, out of the 36 fabricated memory cells, 35 showed excellent WORM behavior with a memory window of 10^4 or higher. The I−V responses of the 35 memory units are depicted in Figure 4e. Evidently, the device yield of device D_1 is 97.22%. Such a high device yield is desirable for commercially viable memory devices.[29] The cumulative probability of V_{SET} of all the 35 cells is presented in Figure 4f, while the cumulative probability of R_{HRS} and R_{LRS} are depicted in Figure 4g. The statistical variation of the various memory parameters of device D_1 is given in Table 1. The above results imply that device D_1 with device structure Au/CAMN1/ITO is an excellent candidate for next generation nonvolatile WORM memory applications.

The I−V response of the device D_2, having structure Au/CAMN2/ITO, has been recorded by applying DC staircase sweeps in the sequence 0 V → −5 V → 0 V → 5 V → 0 V→ −5 V → 0 V. The CC was initially set to an optimized value of 1 mA in both negative and positive polarity, initially. Figure 5a,b depict the typical I−V response of the device D_2, having structure Au/CAMN2/ITO, in linear scale and semi logarithmic scale, respectively, with a CC value set at 1 mA. The sweep direction and sequence are also included in the figures (Figure 5a,b). Here also, the device D_2, was initially found to be at the HRS on application of the first scan (0 V → −5 V) similar to device D_1. However, with the increase in the applied voltage, the device switches from the HRS to the LRS at $V_{SET} = -2.25$ V and retained the LRS state during the return scan -(−5 V → 0 V) similar to device D_1. Moreover, the device D_2 continued to remain in the LRS even under subsequent voltage scans (0 V → 5 V → 0 V → −5 V → 0 V) exhibiting WORM type RS behavior similar to device D_1. The memory window of device D_2 was found to be of the order of 10^4 at a data read out voltage of 0.1 V.

Recently, several researchers have identified that CC may play a crucial role in the switching behavior of RS devices.[18,47] In the present study also, the effects of CC in the RS behavior of the device D_2 have been investigated by gradually raising the CC from 1 to 50 mA at an interval of 1 mA in the positive polarity while keeping the CC fixed at 1 mA in the negative polarity. With CC up to 2 mA, the device showed WORM behavior. However, when the CC was 3 mA, the I−V nature of the device became quite interesting. The corresponding I−V curves are depicted in Figure 5c,d in linear scale and semi logarithmic scale, respectively. Here, the device D_2 switched from the HRS to the LRS during the first voltage scan (0 → −5 V) and maintained the LRS state during the reverse scan (−5 V → 0 V) like the previous cases. However, most interestingly, during the third scan (0 V → 5 V) the device undergoes a transition from the LRS to the HRS at a threshold voltage of 1.45 V. This transition from the LRS to the HRS is known as the RESET process which is equivalent to the "data erasing" process in digital memory.[47] The voltage at which the transition occurs is known as the reset voltage (V_{RESET}).[48] Subsequently, during the fourth scan (5 V → 0 V), the device retained the HRS state. Moreover, the HRS of the device can be reprogrammed to the LRS by applying the voltage scan (0 V → −5 V) again. This kind of RS behavior is suitable for RRAM application where write, read, erase and rewrite operations can be realized by applying appropriate voltage bias.[15,49] Here it is important to note that both states (HRS or LRS) of the device were maintained even after the removal of the external power indicating the stable and nonvolatile nature of the stored information in device D_2. These results suggest that device D_2 with device structure Au/CAMN2/ITO exhibits RRAM behavior with a memory window of the order of 10^4 (@ 0.1 V) when the CC is set to an optimal value of 3 mA or more (up to 50 mA).[15] However, with CC greater than 50 mA, the device active layer got permanently damaged due to Joule's heating.[44] Therefore, the device D_2 can operate in two modes, either in the WORM mode or in the RRAM mode, depending on the measurement protocol (i.e., CC).

The data retention characteristics and read endurance of the device (D_2) have been evaluated for both WORM and RRAM modes by measuring the values of R_{HRS} and R_{LRS} of the device following the same protocol as that followed for device D_1. The corresponding results are shown in Figure 5e and Figure 5f, respectively. As indicated by Figure 5e, device D_2 can also retain the stored information for at least 3×10^4 s. Moreover, the read endurance of device D_2 is found to be at least 10^4.

Cyclibility is one of the most important memory parameters in case of an RRAM device from the application point of view.[46] Cyclibility refers to the number of times the resistance states (HRS and LRS) of the RRAM device can be altered by applying suitable voltage scans.[13,49] In order to assess the cyclibility as well as the cycle -to-cycle (C2C) variation of various memory parameters of the RRAM device (D_2), the I−V response of a particular memory unit in D_2 has been recorded by applying DC staircase sweeps in the sequence 0 V → −5 V → 0 V → 5 V → 0 V, repeatedly for 120 cycles. The obtained I−V response of the RRAM memory unit is depicted in Figure 6a. It has been observed that the particular memory unit can undergo 116 consecutive write-read-erase-read cycles without significant degradation in the memory window. However, during the 117th cycle, the device fails to switch to the LRS and subsequently, remains in the HRS permanently (Figure S4 of the SI). The values of R_{HRS}, R_{LRS},V_{SET}, V_{RESET}, I_{SET} and I_{RESET} have been extracted from the I−V curves and plotted against the number of cycles as shown in Figure 6a, 6b and 6c, respectively, in order to obtain a comprehensive understanding of the temporal (C2C) variation of the various memory parameters. From the graphs (Figure 6b,c,d), it can be observed that the C2C variation of all the memory parameters mentioned above increases with cycle number. This increase in the C2C variation may be due to the degradation of the active layer of the device (D_2) under repetitive voltage stress.[50] The C2C variation increases significantly around the 80th cycle mark as the device moves toward SET failure in the 117th cycle. However, the memory window of the device remains almost unaltered up to the 116th cycle. This indicates that the CAMN2-based RS device can be used for RRAM application for at least up to 116 cycles. Clearly, cyclibility of the present device is 116, which is very good in case of an organic RRAM device.[13] A detailed statistical analysis of the C2C variability of the key performance parameters such as V_{SET}, V_{RESET}, I_{SET}, I_{RESET} R_{HRS} and R_{LRS} of the device D_2 in the RRAM mode of operation is given in tabular form in Table 1. Here, it may be mentioned that, in the case of device D_1, an analysis of C2C variability is immaterial since it exhibits nonreversible WORM behavior only.

For RS devices, it is important to investigate the D2D (spatial) variability of the switching parameters along with the C2C (temporal) variability.[46] In order to assess the D2D variability of device D_2, 36 independent and identical memory units have been prepared in a 6 × 6 array, having a device configuration identical to that of device D_2. Interestingly, all 36 memory units showed excellent WORM as well as RRAM switching behavior depending on the CC with memory window of at least 10^4. I−V curves of all 36 memory cells are shown in Figure S5 of SI. In order to gain a deeper insight into the spatiotemporal (D2D and C2C) variability of the switching parameters of the RRAM device D_2, the values of V_{SET}, V_{RESET}, R_{HRS} and R_{LRS} have been extracted from the I−V curves of the first 30 cycles of each of the 36 memory units of D_2. The spatiotemporal variability of V_{SET} and V_{RESET}, has been depicted in Figure 7a using box-plot. The vertical bars show the temporal variations of V_{SET} and V_{RESET} for a particular device. Similarly, the spatiotemporal variability of R_{HRS} and

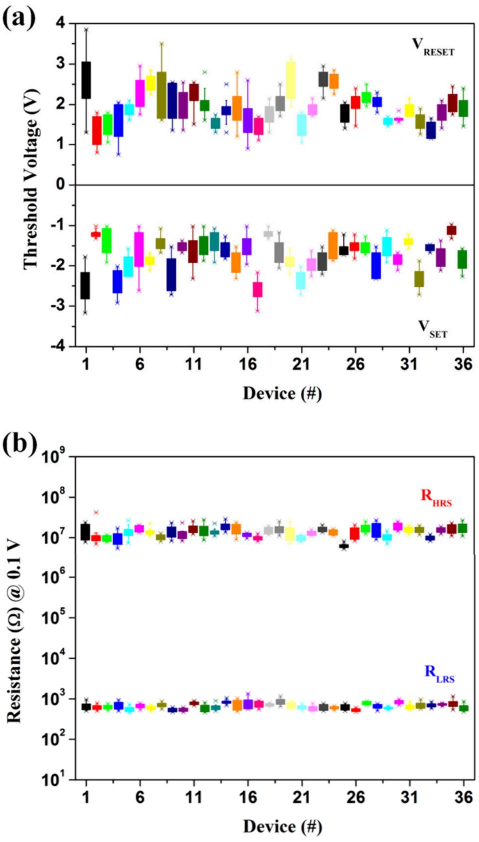

Figure 7. (a) Spatiotemporal variability of V_{SET} and V_{RESET}. of device D_2. (b) Spatiotemporal variability of R_{HRS} and R_{LRS} of device D_2.

Table 2. Device-to-Device Statistical Variation of the Various Memory Parameters of Device D_1 and D_2

memory parameters		device D_1	device D_2	
switching behavior		WORM	WORM	RRAM
V_{SET}	range	−2 V to −3 V	−0.95 V to −3.05 V[a]	−0.95 V to −3.05 V[a]
	mean	−2.63 V	−2.21 V[a]	−2.21 V[a]
	relative deviation	8.46%	26.73%[a]	26.73%[a]
V_{RESET}	range	NA[b]	NA[b]	0.85 to 2.80 V[a]
	mean	NA[b]	NA[b]	2.1 V[a]
	relative deviation	NA[b]	NA[b]	27%[a]
R_{HRS}	range	4.76 MΩ to 27.26 MΩ	4.72 MΩ to 87.11 MΩ[a]	4.72 MΩ to 87.11 MΩ[a]
	mean	13.404 MΩ	23.88 MΩ[a]	23.88 MΩ[a]
	relative deviation	36.13%	41%	41%
R_{LRS}	range	202 Ω to 395 Ω	309.5 Ω to 1034.2 Ω[a]	309.5 Ω to 1034.2 Ω[a]
	mean	278.9 Ω	652.6 Ω[a]	652.6 Ω[a]
	relative deviation	17.62%	22.08%[a]	22.08%[a]
memory window		~10^4	~10^4	~10^4
cyclibility		NA[a]	NA[a]	116
read endurance		10^4	10^4	10^4
retention time		3 × 10^4	3 × 10^4	3 × 10^4
device yield		97.22%	100%	100%

[a]values extracted from first switching cycle of all the memory cells [b]not applicable.

Table 3. Performance Comparison of Various OSM-Based RS Devices

Sl. No.	Device configuration	Switching Behavior	V_{SET} (V)	V_{RESET} (V)	retention time	read endurance	cyclibility	memory window	device yield	ref
01	Al/BHEPDQ/ITO	RRAM	2.26 V	−2.88 V	10^4 s	ND	ND	100	ND	60
02	Al/Py-Fc/ITO	RRAM	−1.6	3 V	2 × 10^3 s	ND[b]	10^3	10^4	80%	56
03	Ag/triarylamine and benzophenone/ITO	WORM	−0.82	NA[a]	10^3	ND	NA	$10^{2.}$	100%	23
04	Ag/Functionalized Bis (triphenylamine)/ITO	WORM	−1.19	NA	10^3 s	10^2	NA	10^3.	ND	57
05	Al/BODIPY?ITO	WORM	2.6 to 3.5	NA	8500	ND	NA	10^5	ND	27
06	Ag/TAA-quinoline/ITO	WORM	−1.21 to −2.12	NA	10^3	10^2	NA	10^5	ND	58
07	Au/Indole1/ITO	RRAM	−2.45	2.58	5.4× 10^3 s	ND	50	10^6	86.7%	13
08	Al/7HNO3C/ITO	WORM	1.67	NA	4 × 10^3 s	1270	NA	10^2	ND	11
09	Ag/phenazine and quinoxaline-derrivatives/ITO	WORM	−0.74	NA	10^3 s	100	NA	10^3 to 10^4	ND	9
10	Ag/benzothiadiazole-derivatives/ITO	WORM	−0.80 V	NA	10^3 s	10^2	NA	~10^2	ND	59
11	Au/CAMN1/ITO	WORM	−2.45	NA	3 × 10^4	10^4	NA	10^4	97.22%	#[c]
12	Au/CAMN2/ITO	RRAM	−2.25	1.45	3 × 10^4	10^4	116	10^4	100%	#
		WORM	−2.25	NA	3 × 10^4	10^4	NA	10^4	100%	

[a]NA = not applicable. [b]ND = no data. [c]#this work.

R_{LRS}, has been depicted in Figure 7b with the vertical bars representing the temporal variation of R_{HRS} and R_{LRS}, respectively. As observed from Figure 7a, all 36 memory cells in D_2 show a significant temporal variation in V_{SET} and V_{RESET} values. However, the temporal variation for R_{HRS} and R_{LRS}, values of all 36 memory cells (Figure 7b) is negligible, indicating the spatiotemporal stability of both resistance states (HRS and LRS) of the CAMN2-based RRAM device. Here, it may be noted that the higher temporal variation in V_{SET} and V_{RESET} may be due to the fatigue induced in the device active layer under repeated voltage stress.[13,46] Statistical variations of the memory parameters of device D_2 are also represented in Table 2.

The above results clearly indicate that both devices (D_1 and D_2) show excellent RS memory behavior with outstanding device yield of 97.22% and 100%, respectively, which is very important from a commercial application point of view. The device D_1 with CAMN1 as active material exhibits WORM type memory behavior, whereas the device D_2 with CAMN2 as the active layer shows both WORM and RRAM type RS behavior. Over the past decade, significant progress has been made in the organic small molecule (OSM)-based resistive switching technology.[5,7−9,11−13,23,32,35] A number of OSMs has been reported in the literature which may contribute significantly in the next-generation organic electronic technology.[9,11,13,23,27,28,51−60] In this regard, it is important to assess the performance of the proposed coumarin-based devices (D_1 and D_2) in comparison with the previously reported OSM-based devices. Table 3 provides a comprehensive and fair comparison of the memory performance of both devices D_1 and D_2, with the previously reported OSM-based devices.

A close look at Table 3 reveals that both devices D_1 and D_2 exhibit comparable RS performance with the earlier reported studies on OSM-based devices in terms of cyclibility and

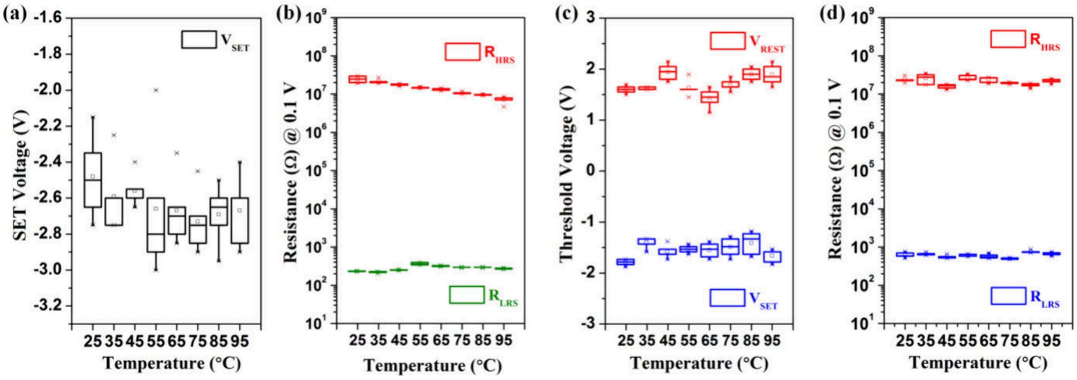

Figure 8. (a) Variation of V_{SET} of D_1 with temperature. (b) Variation of R_{HRS} and R_{LRS} of D_1 with temperature. (c) Variation of V_{SET} and V_{RESET} of D_2 with temperature. (d) Variation of R_{HRS} and R_{LRS} of D_2 with temperature.

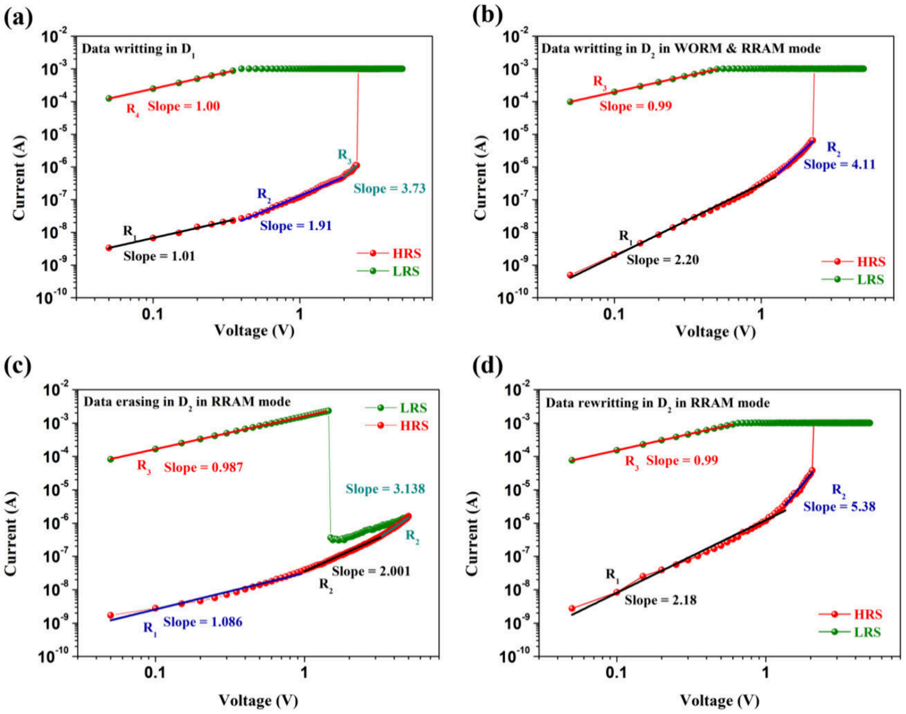

Figure 9. Double logarithmic plot of the typical I−V response of (a) device D_1, (b) device D_2, during data writing or SET process in both WORM and RRAM mode of operation. (c) device D_2, during data erasing or RESET process in RRAM mode of operation. (d) device D_2, during the data rewriting process in RRAM mode of operation.

memory window. However, both CAMN1- and CAMN2-based devices show a greater retention time compared to the earlier reported OSM-based RS memory. Moreover, read endurance and device yield, which are very important performance parameters for a commercially viable memory device, are rarely studied. In the current study, the read endurance and the device yield of devices D_1 and D_2 have been thoroughly investigated. Read endurance of both devices has been found to be on the order of 10^4, which is excellent from an application point of view. Moreover, both devices D_1 and D_2 exhibited very high device yield (97.22% and 100%, respectively), which is important for effective commercialization.

Although OSM-based RS devices show promising results as viable candidates for electronics technology, the long-term physical stability as well as thermal stability still remains a point of concern.[61,62] Hence, it becomes important to analyze the physical and thermal stability of the proposed coumarin-based devices. Here, the long-term physical stability of devices D_1 and D_2 has been investigated by recording the I−V data of both devices for an extended period of time. The obtained I−V curves, depicted in Figures S6 and S7, respectively, clearly revealed that device D_1 showed reproducible WORM behavior even after 400 days of fabrication, whereas the device D_2 showed reliable WORM and RRAM behavior for the same duration. However, both the devices continued to show their respective RS behavior even beyond this period of measurement.

The thermal stability of the coumarin-based devices (D_1 and D_2) has been investigated by recording the I−V response of both devices with increasing temperature starting from 25 to 95 °C at an interval of 10 °C. It was observed that both devices showed their respective RS behavior even at higher temperatures, indicating excellent thermal stability. For a comprehensive assessment of the performance of both devices at higher temperatures, the I−V response of five separate memory units were recorded for each temperature for both devices. The values of V_{SET} and V_{RESET}, extracted from the I−V curves of D_1 and D_2, have been depicted in Figure 8a,c, respectively, whereas the values of R_{HRS} and R_{LRS} have been plotted in Figure 8b,d, respectively. As observed from Figure 8a, the variation of V_{SET} for D_1 falls well within the D2D variability of the device. Similarly, the variation in V_{SET} and V_{RESET} for D_2 falls well within the spatiotemporal variability of the device (Figure 8c). Similar behavior has been observed in a previously reported coumarin-based device.[13] Moreover, the values of R_{HRS} and R_{LRS} of device D_2 have been found to vary randomly with increasing temperature, which is well within the spatiotemporal variability of the device. The temperature independent variability in R_{HRS} and R_{LRS} values of D_2 is indicative of the semiconducting nature of the device.[29] Similar variations have been observed in the R_{LRS} values of the CAMN1-based device D_1 (Figure 8b) indicating the semiconducting nature of the LRS of the device. However, interestingly, the values of R_{HRS} (@ 0.1 V) of device D_1 show a decreasing trend, on average, with increasing temperature (Figure 8b). This decrease in the R_{HRS} values may be due to the presence of a higher number of thermally generated charge carriers in the device active layer at low applied bias.[11,29,63] This is explored further in a later section of the manuscript. Clearly, both devices show significantly high physical and thermal stability which are extremely important from an application point of view. The above results clearly reveal that both devices hold significant potential to play a major role in next generation electronics technology.

In order to evaluate the performance of the proposed resistive switching memory devices (D_1 and D_2) comprehensively, it is important to analyze the conduction as well as the resistive switching mechanisms of the devices. In recent years several conduction and switching mechanisms, such as space-charge-limited-conduction (SCLC), charge tunneling and hopping, trapping-detrapping, Schottkey emission, Poole-Frankel emission etc., have been proposed for OSM-based resistive switching devices.[64−67] In the present case, the conduction mechanisms of the coumarin-based devices (D_1 and D_2) have been investigated by replotting the I−V data of the devices in double-logarithmic scale and identifying the I−V relationship at various voltage ranges using linear fitting method.[11] Figure 9 shows the linear fitting results in the double-logarithmic plot of the I−V responses of devices D_1 and D_2 in different operating modes. As evident from Figure 9a, three distinct regimes can be identified in the I−V response of the HRS of device D_1. In regime R_1, (0.05 to 0.15 V, slope = 1.01) Ohmic conduction ($I \propto V^1$) is observed, which may be due to thermally generated electrons in the device's active layer at low applied voltage. This assessment also aligns with the fact that at low voltage (0.1 V), the resistance of the HRS of device D_1 decreases with increasing temperature (Figure 8b). Here, as the temperature increases, a larger number of electrons are liberated in the active layer as they gain sufficient energy and consequently contribute to the current conduction. Regime R_2 (0.15 to 1.95 V) is characterized by a slope value of 1.91 (~2), indicating that the I−V response obeys Child's law ($I \propto V^2$). This type of quadratic I−V relation is observed when the number of charge carriers injected from the electrode dominates the number of thermally generated electrons in the active layer. Consequently, in this regime (R_2), the current conduction is mainly due to the injected charge carriers and controlled by the charge traps present in the active layer.[68,69] The oxygen atoms present in the coumarin scaffold may act as trap centers for the injected charge carriers. Here, initially, the injected charge carriers are trapped in the charge traps present in the active layer. However, with the increase of applied bias, the charge traps present in the active layer begin to fill up rapidly which is characterized by a sharp rise in slope value in regime R_3 (1.95 to 2.45 V, slope = 3.73). As the applied bias increases further, all the traps, present in the active layer, get filled up completely, forming a conducting channel. As a result, the device switches to the LRS exhibiting an Ohmic ($I \propto V^1$) I−V relationship (regime R_4, slope = 1). The linear fitting of the double logarithmic I−V curves for device D_2 in WORM mode and the first cycle (SET or data writing process) of RRAM mode is shown in Figure 9b. Here, even at low bias, current in the device (D_2) follows Child's law ($I \propto V^2$) in regime R_1 (0.05−1.25 V), characterized by a slope value of 2.2. Clearly, current conduction in the HRS of device D_2 is largely dominated by the charge carriers injected from the electrodes and controlled by the charge traps even at a lower applied bias. Similar to device D_1, as the applied bias is increased, the charge traps present in the active layer of device D_2 begins to fill up rapidly and a sharp rise in the slope value (slope = 4.11) is observed in regime R_2 (1.25 to 2.25 V) of the HRS of device D_2. With a further increase in the applied bias, the charge traps are filled up completely forming a conduction channel and the device D_2 switches from the HRS to the Ohmic ($I \propto V^1$) LRS with a slope value of 0.99 (regime R_3). Figure 9c depicts the linear fitting results of the RESET (data erasing) process of device D_2 in the RRAM mode. As observed from the figure, the LRS of the device (regime R_4) exhibits Ohmic conduction (slope = 0.987) up to the reset voltage of 1.45 V after which the device exhibits SCLC conduction (in the HRS state) with characteristic slope values of 1.086 (0.05 V to 1 V), 2.001 (1.05 V to 3.30 V) and 3.138 (3.35 V to 5 V) in regime R_1, R_2 and R_3, respectively. The conduction mechanism of device D_2 during the "data rewriting" process in RRAM mode is analyzed from the linear fitting results presented in Figure 9d. It is interesting to note that during the "data rewriting" process also the device exhibits SCLC mechanism similar to that during the "data writing" process or the first switching cycle of the device with slightly different slope values (2.18 in regime R_1 and 5.38 in regime R_2) at the HRS of the device. The above analysis of the double logarithmic graphs of the I−V response of the devices (D_1 and D_2) clearly indicates that the conduction mechanism in both devices (D_1 and D_2) is dominated by a trap-controlled SCLC mechanism.[29,64,70] The nature of the charge carriers and the traps are further explored in later sections of the manuscript. Here, it is interesting to note that, unlike device D_1, the HRS of device D_2 does not exhibit Ohmic conduction at low applied voltages during the SET process. The absence of an Ohmic slope in the HRS indicates the absence of thermally generated charge carriers at low applied bias in device D_2. This assessment is consistent with the fact that, in the case of device D_2, the HRS resistance (at low applied bias) does not decrease with temperature predominantly (Figure 8d) like that in the case of device D_1 (Figure 8b).

The Ohmic nature of the LRS of both devices (D_1 and D_2) is indicative of the presence of conductive filaments in the LRS of the devices. The nature of such filaments can be evaluated by assessing the variation of LRS resistance (R_{LRS}) with the temperature. As per earlier reports, a monotonic increase in R_{LRS} with increasing temperature may indicate the metallic nature of such filaments.[11,71] However, as discussed earlier, the value of R_{LRS} has been found to vary randomly with increasing temperature for both devices (Figure 8b,d). Moreover, in this study, we have utilized Au as the top electrode in both devices. Since Au is a novel metal, formation of Au filaments due to electrochemical metallization is very rare. These observations clearly regress the possibility of metallic filament formation in the LRS of both devices. On the other hand, recent studies have identified that intra- and intermolecular charge transfer (ICT) process play a crucial role in the switching behavior of RS devices-based on OSMs with donor-π-acceptor (D-π-A) configuration.[7,9,11,21,23,28,32,62] Typically, it has been observed that in the ground state of the molecule, the highest occupied molecular orbital (HOMO) is situated within the donor region of the molecule. Conversely, in the excited state, especially when a charge transfer (CT) process occurs, the lowest unoccupied molecular orbital (LUMO) tends to be found in the acceptor region of the molecule.[11,23,57]

In the present case also, the ICT process may play a crucial role in the RS mechanism of devices D_1 and D_2 where CAMN1 and CAMN2, having a D-π-A configuration, act as the active layers, respectively. Here, DFT-based calculations have been carried out in view of comprehending the involvement of ICT process in the RS behavior of both devices D_1 and D_2. The molecular orbital energy levels as well as the electrostatic potential surface (ESP) diagrams of CAMN1 and CAMN2, obtained from DFT calculations, are depicted in Figure 10a,b, respectively. As observed from the Figure 10a, in the ground state of the molecules (CAMN1 and CAMN2), the HOMO orbitals are primarily located at the electron-donor part of the molecules. On the other hand, the LUMO orbitals are mainly located over the coumarin scaffold which is attributed to the electron-accepting nature of the coumarin scaffold as a whole. Now, when voltage sweep (0 V to −5 V) is applied, the electrons in the HOMO level starts to accumulate sufficient energy and transfer to the LUMO of the molecules in the excited state and subsequently form a charge transfer (CT) complex.[23,28] The creation of the CT complex leaves behind a large number of holes in the HOMO level (electron-donor part) of the molecules.[23,28] Now, as the applied bias approaches the V_{SET} values of the devices, the holes, created during the CT process, form an open conductive channel through the delocalizations in the donor parts of the molecules and subsequently drive the devices to their corresponding LRS.[7,23,28] Moreover, both CAMN1 and CAMN2 exhibit comparatively high dipole moment (3.465 and 7.853 D, respectively). This high dipole moment stabilizes the CT complexes which results in the observed long retention time (Figure 4e and 5e, respectively) in both devices.[9,23,28] Moreover, the role of the ICT process can be further substantiated by UV−vis spectroscopic analysis of the active layers (CAMN1 and CAMN2) of devices D_1 and D_2.[72] Figure S8a,b shows the UV−vis spectra of CAMN1 and CAMN2 in solution state (chloroform) and in spin-coated thin film, respectively. As observed from Figure S8a, both CAMN1 and CAMN2 show prominent peaks at around 320 nm, whereas no prominent peaks were observed at lower energy bands. However, it is interesting to note that, in spin-coated thin films, both CAMN1 and CAMN2 show significant absorption at lower energy bands (Figure S8b). The existence of such absorption bands in the spin-coated films of the compounds may be attributed to the formation of CT complexes in thin film state due to the intramolecular charge transfer process from the electron-donor part of the molecules to electron-accepting coumarin scaffold in case CAMN1 and due to the intermolecular charge transfer process from the electron-donor part of one molecule of CAMN2 to the electron-accepting part of a neighboring CAMN2 molecule.[72] Moreover, due to the presence of the strongly donating -OCH_3 group, CAMN2 forms strong intermolecular CT complexes in thin film state.[23] In order to explore this further, we have studied the solvent dependent nature of the absorption spectra of both CAMN1 and CAMN2 in three solvents having different polarities, namely, chloroform, toluene, and dichloromethane. The absorption spectroscopy results are shown in the Figure S9 of the SI. As observed from Figure S9, both CAMN1 and CAMN2 molecules do not show any shift in the absorption peak positions with respect to the variation in solvent polarity. This indicates that the nature of the charge transfer for CAMN1 and CAMN2 compounds are independent of solvent polarity. Moreover, the spin-coated thin films of both compounds (Figure S8b) exhibit significant absorption at lower-energy bands. In particular, the spin-coated thin film of CAMN2 exhibits a broad absorption peak in the lower energy bands indicating the formation of strong charge transfer complexes in the solid state where the molecules are closely packed due to dipole−dipole interactions among the neighboring molecules.[73,74] However, because they are in the solution state, the molecules are separated from one another by the solvent molecules, and the dipole−dipole interaction is significantly reduced.[75] As a result, in the solution state, both CAMN1 and CAMN2 compounds do not show significant absorption in the lower energy bands. Moreover, the presence of -OCH_3 in CAMN2 group plays a crucial role during the RESET process of the CAMN2-based RRAM device D_2. This has been explored in detail in later sections of the manuscript.

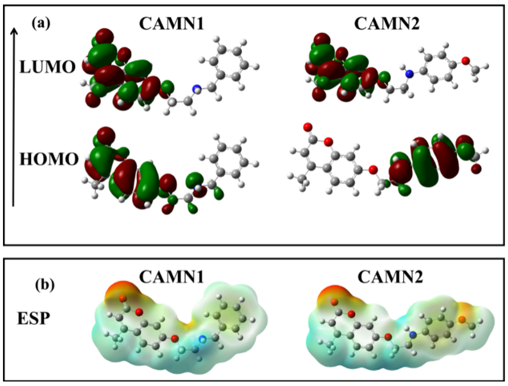

Figure 10. (a) HOMO and LUMO orbitals of CAMN1 and CAMN2. (b) ESP diagrams of CAMN1 and CAMN2.

In order to probe deeper into the switching mechanism of the devices, we analyzed the electrochemical properties of both CAMN1 and CAMN2 compounds using cyclic voltammetry experiments. Cyclic voltametric analysis of both compounds were carried out with DMSO as solvent. Both compounds were examined in the solution phase with 50 mM tetrabutylammonium hexafluorophosphate DMSO solution as the supporting electrolyte at a scan rate of 100 mV/s. Platinum electrode was used as the working electrode in both cases. Ag/AgCl electrode and a platinum wire were used as the reference

Table 4. Electrochemical Properties of CAMN1 and CAMN2 Compounds

Compound	DFT			Cyclic Voltammetry		
	HOMO	LUMO	Band Gap (E_g)	HOMO	LUMO	Band Gap (E_g)
CAMN1	−5.962 eV	−1.507 eV	4.455 eV	−5.924 eV	−1.465 eV	4.459 eV
CAMN2	−5.799 eV	−1.478 eV	4.321 eV	−5.788 eV	−1.637 eV	4.151 eV

and the counter electrode, respectively. Ferrocene was used as the external standard for calibrating the potential and estimating HOMO−LUMO energy levels.[76] Figure S10a,b shows the cyclic voltammograms of CAMN1 and CAMN2, respectively. The values of HOMO (E_{HOMO}), LUMO (E_{LUMO}) and energy band gap (E_g) obtained from the cyclic voltamograms (details are mentioned in the SI) are summarized and compared with their computational counter parts (obtained from the DFT calculations) in Table 4.[77] As observed from Table 4, the values of E_{HOMO}, E_{LUMO} and E_g obtained from theoretical (DFT) calculators closely correlate with their experimentally obtained counter parts. To comprehend the nature of the charge carrier transport across the device active layer, an energy level diagram of the HOMO and LUMO levels of the compounds is plotted and compared with the work functions of the Au and ITO electrodes, as shown in Figure 11. As observed from Figure 11, both CAMN1 and CAMN2 exhibit significantly lower hole injection barrier (1.224 and 1.088 eV, respectively) between the ITO bottom electrode and the HOMO levels of the active layers compared to the electron injection barrier between the Au top electrode and the LUMO of the active layers of both devices D_1 and D_2, (3.635 and 3.463 eV, respectively). Therefore, hole injection from the ITO bottom electrode to the HOMO of the active layers of the devices, under a negative voltage sweep, dominates the conduction process in both devices. Notably, the slightly larger hole injection barrier for D_1 compared to that of D_2 (Figure 11) may contribute to the observed higher value of V_{SET} for D_1. Moreover, the energy band gap for CAMN1 is found to be slightly greater than that of CAMN2 (Figure 11) which may also be responsible for the higher V_{SET} for D_1.

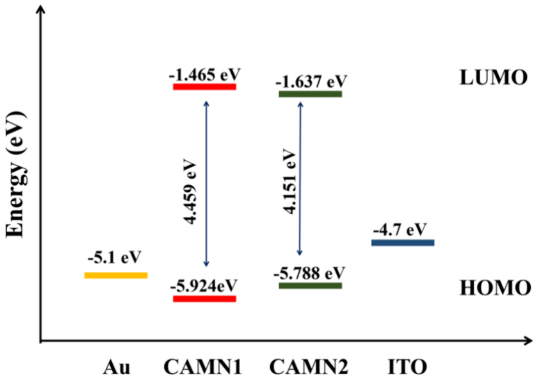

Figure 11. Energy level diagrams of CAMN1and CAMN2 with the work functions o the electrodes.

In previous sections of the paper, we have found that trap-controlled SCLC is the key mechanism behind current conduction in the HRS of both devices. In this regard, ESP diagrams (Figure 10b), obtained based on the Merz−Kollmann potential, may provide significant insights into the nature of the charge traps.[78] The ESP diagrams show a shift in color (from blue to red) with an increasing electron density. As observed from the ESP diagrams (Figure 10b), a significant negative ESP is observed over the "=O" region of the coumarin scaffold of both molecules which may be attributed to the lone electron pair of the oxygen molecules. Moreover, a slightly negative ESP is also observed over the "-O-" regions of both molecules. These negative ESP regions, present in the molecules, show strong affinity toward the holes injected from the ITO bottom electrode under negative voltage sweep and act as charge traps within the active layer of the device. Furthermore, the slightly positive ESP regions spread over the entire molecular backbone may provide a smooth pathway for hole transport along the molecular framework.

Moreover, the observed difference in the RS behavior of the devices D_1 and D_2 may be due to the presence of the $-OCH_3$ group in the donor part of the CAMN2 molecule. In order to explore the role of the methoxy ($-OCH_3$) group in defining the resistive switching behavior of the devices, we consider the HOMO and LUMO energy levels and isosurfaces and ESP diagrams of both CAMN1 and CAMN2 molecules presented in Figure 10a and 10b, respectively. As observed from the Figure 10a, the LUMO orbitals of both molecules (CAMN1 and CAMN2) are primarily located over the entire coumarin scaffold which is attributed to the electron-accepting nature of the coumarin scaffold as a whole. However, a significant difference is observed in the positions of the HOMO orbitals of CAMN2 with respect to CAMN1. The HOMO orbital is spread over the molecular backbone of CAMN1, while the HOMO orbital of CAMN2 molecule is localized densely over the methoxybenzene moiety creating a greater charge separated state for CAMN2 as compared to that of CAMN1. Due to the large charge separation between HOMO and LUMO of CAMN2, it possesses a stronger dipole moment (7.853 debye, obtained from DFT calculations) compared to CAMN1 (3.465 debye, obtained from DFT calculations). This difference in the dipole moment of the molecules (CAMN1 and CAMN2) plays a crucial role in determining the nature of the self-assembly of the molecules in spin-coated thin films by adjusting the relative orientation of the molecules.[74] Due to the high dipole moment of CAMN2 molecule, stronger dipole−dipole interactions may take place among the neighboring molecules in CAMN2 thin film compared to that in CAMN1 thin film.[79] As a result of this strong dipole−dipole interaction, CAMN2 molecules tend to form strong intermolecular charge transfer complexes where the negative pole of one CAMN2 molecule is closely packed with the positive pole of a neighboring CAMN2 molecule forming a three-dimensional spherical microstructure as observed from the SEM images of CAMN2 spin-coated films in Figure 3a. On the other hand, due to weaker dipole moment, CAMN1 molecules do not exhibit such strong dipole−dipole interaction and tend to self-assemble along the orientation of dipolar moments to form a 3-dimensional rodlike microstructure as observed from the SEM image of the spin-coated thin film of CAMN1 shown in Figure 3b.[80] Due to such molecular organization, CAMN1 tends to form intramolecular charge transfer complexes, where charge is transferred from the HOMO to the LUMO of the same molecule, instead of forming intermolecular charge transfer complexes where charge is transferred from the HOMO of one molecule to the LUMO of a neighboring molecule as observed in case of CAMN2.[74] Accordingly, the energy required for the HOMO−LUMO intramolecular charge transfer (in the case of CAMN1) is comparatively larger than the energy required for the HOMO−LUMO intermolecular charge transfer (in the case of CAMN2). This is because the HOMO−LUMO energy gap is less for the intermolecular charge transfer than that for the intermolecular charge transfer. As a result, device D_1 requires more energy to transit from the HRS to LRS compared to device D_2. This observation also agrees with the fact that the value of VSET for D_1 (−2.45 V) is larger than that of D_2 (−2.25 V).

Now, in the case of device D_2, when CC is increased beyond 3 mA, due to excessive flow of current, a large number of charge carriers are injected into the active layer of the device which may disrupt the stability of the intermolecular charge transfer complexes formed within the CAMN2 thin film. As a result, the hole-mediated conductive pathways formed during HRS to LRS transition (during scan 0 V to −5 V) within the CAMN2 thin film is ruptured, the device undergoes LRS to HRS transition (during scan 0 V to 5 V, CC = 3 mA) and the device D_2 exhibits RRAM behavior. On the other hand, in case of device D_1, the intramolecular charge transfer complex formed within the CAMN1 molecule during the HRS to LRS transition, remain unaffected even when a large number of charge carrier is injected into the CAMN1 thin film. Consequently, once switched to the LRS from the HRS, device D_1 remains in the LRS, permanently, even when compliance is increased beyond 3 mA showing WORM type resistive switching.

IV. CONCLUSION

In conclusion, ORS memory devices having structures Au/CAMN1/ITO and Au/CAMN2/ITO have been fabricated using synthesized coumarin derivatives 7-(2-(benzylamino)-ethoxy)-4-methyl-2H-chromen-2-one and 7-(2-(4-methoxyphenylamino)ethoxy)-4-methyl-2H-chromen-2-one. The surface morphology of the spin-coated active layer of the devices has been investigated using FESEM which reveals the formation of well connected structure for both devices. The CAMN1-based device exhibited WORM type RS behavior, while the CAMN2-based device showed both WORM as well as RRAM RS behavior depending on compliance current. The device yields of the designed ORS have been found to be 97.22% and 100%, respectively, for the CAMN1 and CAMN2-based devices. The read endurance and the data retention time was found to be 10^4 and 3×10^4 s, respectively, for both devices. Moreover both the devices exhibited superior physical stability of at least 400 days as well as thermal stability up to 95 °C. DFT-based calculations as well as absorption spectroscopic studies revealed that the intra/intermolecular charge transfer phenomenon was mostly responsible for the observed RS behavior of both the devices, while trap-controlled SCLC mechanism was responsible for the current conduction in both cases. It was found that the presence of the methoxy ($-OCH_3$) group in the CAMN2 molecule and the absence of the same in the CAMN1 molecule is the key reason behind the observed difference in the RS behaviors of the two molecules. Moreover, in the RRAM mode of operation, the CAMN2-based device was found to have a cyclibility of 116 cycles, that is, the device could undergo at least 116 continuous write-read-erase-read-rewrite operations after which the device remained in the "OFF" state permanently. This cyclability can be further improved by addressing the degradation of the active layer material under a constant voltage stress. This may be done by introducing various matrix materials (such as fullerene) within the device active layer or by modifying the molecular structure of the coumarin derivative. Work is going on in these directions in our laboratory.

■ ASSOCIATED CONTENT

Supporting Information

The Supporting Information is available free of charge at https://pubs.acs.org/doi/10.1021/acsomega.4c09849.

> Figure S1. (a,b) 1H - NMR and 13C - NMR spectra, respectively, of CAMN1; Figure S2. (a,b) 1H - NMR and 13C - NMR spectra, respectively, of CAMN2; Figure S3. I−V response of device D_1 on semi logarithmic scale when compliance current in the positive sweep direction is kept at 50 mA; Figure S4. I−V response of the 117th switching cycle of a particular memory cell in device D_2; Figure S5. Device yield of device D_2; Figure S6. I−V response of device D_1 measured over 400 days; Figure S7. I−V response of device D_2 measured over 400 days; Figure S8. (a) UV−vis spectra of CAMN1 (blue plot) and CAMN2 (red plot) in chloroform solution. (b) UV−vis spectra of CAMN1 (blue plot) and CAMN2 (red plot) in spin coated thin films. Figure S9: UV−vis absorption spectra of CAMN1 and CAMN2 in various solvents. Figure S10. (a) Cyclic voltamograms of spin-coated (a) CAMN1 and (b) CAMN2 thin films (PDF)

■ AUTHOR INFORMATION

Corresponding Author

Syed Arshad Hussain − *Thin Film and Nanoscience Laboratory, Department of Physics, Tripura University, 799022 West Tripura, Tripura, India;* orcid.org/0000-0002-3298-6260; Phone: +91940212250; Email: sa_h153@hotmail.com, sahussain@tripurauniv.ac.in; Fax: +913812374802

Authors

Rahul Deb − *Thin Film and Nanoscience Laboratory, Department of Physics, Tripura University, 799022 West Tripura, Tripura, India*

Hritinava Banik − *Thin Film and Nanoscience Laboratory, Department of Physics, Tripura University, 799022 West Tripura, Tripura, India*

Utpal Chandra De − *Department of Chemistry, Tripura University, 799022 West Tripura, Tripura, India*

Debajyoti Bhattacharjee − *Thin Film and Nanoscience Laboratory, Department of Physics, Tripura University, 799022 West Tripura, Tripura, India;* orcid.org/0000-0003-2105-1889

Khuloud A. Alibrahim − *Department of Chemistry, College of Science, Princess Nourah bint Abdulrahman University, Riyadh 11671, Saudi Arabia*

Abdullah N. Alodhayb − *Research Chair for Tribology, Surface, and Interface Sciences, Department of Physics and Astronomy, College of Science, King Saud University, Riyadh 11451, Saudi Arabia;* orcid.org/0000-0003-0202-8712

Complete contact information is available at:
https://pubs.acs.org/10.1021/acsomega.4c09849

Author Contributions

S.A.H. and R.D. designed the work. R.D. and H.B. performed all the experiments. R.D. performed all the data analysis. R.D. performed the DFT calculations. U.C.D synthesized the molecules. R.D. and S.A.H. wrote the manuscript with inputs from U.C.D, K.A.A, A.N.A. and D.B. All the photographs in the manuscript are obtained by R.D.

Notes

The authors declare no competing financial interest.

■ ACKNOWLEDGMENTS

The author S.A.H. is grateful to DST (No. CRG/2021/004073) and CSIR (No.03/1504/23/EMR-II) for the financial support to carry out this research work. The authors are also grateful to CSIR for the financial support to Mr. Hritinava Banik via CSIR- SRF (Direct) award vides File. No. 09/0714(19042)/2024-EMR-I to carry out this research work. The authors acknowledge the central instrumentation center (CIC), Tripura University, for providing the FESEM and NMR facilities. The authors express their gratitude to Princess Nourah bint Abdulrahman University Researchers Supporting Project number (PNURSP2025R92), Princess Nourah bint Abdulrahman University, Riyadh, Saudi Arabia. The author ANA is grateful to the Deanship of Scientific Research, King Saud University, for funding the research through the Vice Deanship of Scientific Research Chairs.

■ REFERENCES

(1) Ullah, I.; Khan, I. U.; Ouaissa, M.; Ouaissa, M.; Hajjami, S. E. *Future Communication Systems Using Artificial Intelligence, Internet of Things and Data Science*, 1st ed.; CRC Press: Boca Raton, 2024. DOI: 10.1201/9781032648309.

(2) Zhang, G.-X.; Zhang, Z.-C.; Chen, X.-D.; Kang, L.; Li, Y.; Wang, F.-D.; Shi, L.; Shi, K.; Liu, Z.-B.; Tian, J.-G.; Lu, T.-B.; Zhang, J. Broadband Sensory Networks with Locally Stored Responsivities for Neuromorphic Machine Vision. *Sci. Adv.* **2023**, *9* (37), No. eadi5104.

(3) Ishimaru, K. Challenges of Flash Memory for Next Decade. In *2021 IEEE International Reliability Physics Symposium (IRPS)*; IEEE: Monterey, CA, USA, 2021; pp 1−5. DOI: 10.1109/IRPS46558.2021.9405182.

(4) Prime, D.; Paul, S. Overview of Organic Memory Devices. *Philos. Trans. R. Soc. A* **2009**, *367* (1905), 4141−4157.

(5) Awais, M.; Zhao, F.; Cheong, K. Y. Bio-Organic Based Resistive Switching Random-Access Memory. *SSP* **2023**, *352*, 85−93.

(6) Nguyen, T. H. V.; Shaikh, M. T. A. S.; Jeon, H. J.; Vu, T. T. H.; Prasad, C. V.; Labed, M.; Kim, S.; Rim, Y. S. Bioresorbable Resistive Switching Device Based on Organic/Inorganic Hybrid Structure for Transient Memory Applications. *Adv. Elect Materials* **2024**, *10* (5), No. 2300759.

(7) Gayathri, R.; Akshaya, M.; Imran, P. M.; Nagarajan, S. Design of Triphenylamine-based D-π-A Systems for Efficient Ternary WORM Memory Devices. *Chem.—Eur. J.* **2024**, *30* (48), No. e202402015.

(8) Sarkar, S.; Banik, H.; Rahman, F. Y.; Majumdar, S.; Bhattacharjee, D.; Hussain, S. A. Effect of Long Chain Fatty Acids on the Memory Switching Behavior of Tetraindolyl Derivatives. *RSC Adv.* **2023**, *13* (38), 26330−26343.

(9) Gayathri, R.; Akshaya, M.; Imran, P. M.; Nagarajan, S. Modified Donor End Caps for Binary-to-Ternary WORM Memory Conversion in N-Heteroaromatic Systems. *ChemPhysChem* **2024**, *25* (11), No. e202400062.

(10) Bhaumik, M.; Maity, A.; Brink, H. G.; Dlamini, Z. W.; Vallabhapurapu, S. Resistive Switching Behaviour of Nickel Nanoparticle-Embedded Naphthalene Sulphonic Acid-Doped Polyaniline Nanocomposites. *J. Phys. D: Appl. Phys.* **2024**, *57* (4), No. 045302.

(11) Deb, R.; Rahman, F. Y.; Sarkar, S.; Banik, H.; Paul, P. K.; Bhattacharjee, D.; Alibrahim, K. A.; Alodhayb, A. N.; Hussain, S. A. ZnO Nanoparticle-Induced Performance Enhancement of a Coumarin-Based Nonvolatile Memory Device. *ACS Appl. Eng. Mater.* **2024**, *2* (4), 1141−1152.

(12) Banik, H.; Sarkar, S.; Bhattacharjee, D.; Malhotra, A.; Chauhan, A.; Hussain, S. A. Noncytotoxic WORM Memory Using Lysozyme with Ultrahigh Stability for Transient and Sustainable Electronics Applications. *ACS Omega* **2024**, *9* (1), 618−627.

(13) Sarkar, S.; Banik, H.; Suklabaidya, S.; Deb, B.; Majumdar, S.; Paul, P. K.; Bhattacharjee, D.; Hussain, S. A. Resistive Switching of the Tetraindolyl Derivative in Ultrathin Films: A Potential Candidate for Nonvolatile Memory Applications. *Langmuir* **2021**, *37* (15), 4449−4459.

(14) Wang, S.; Sun, Z. Dual In-Memory Computing of Matrix-Vector Multiplication for Accelerating Neural Networks. *Device* **2024**, *2* (12), No. 100546.

(15) Dey, B.; Sarkar, S.; Banik, H.; Arshad Hussain, S. Resistive Switching Behaviour of Organic Molecules. *Materials Today: Proceedings* **2021**, *46*, 6290−6294.

(16) Han, G.; Seo, J.; Lee, K.; Kim, D.; Seo, Y.; Lee, J.; Choi, J.; Ahn, D.; Oh, S.; Hwang, H. Highly Scalable Vertical Bypass RRAM Using Interface-Type Resistive Switching Mechanism for V-Nand Memory Applications. *IEEE Trans. Electron Devices* **2024**, *71* (12), 7970−7977.

(17) Harnack, N.; Rodehutskors, S.; Gotsmann, B. Scanning Thermal Microscopy Method for Self-Heating in Non-Linear Devices and Application to Current Filaments in Resistive RAM. *arXiv*, Sept. 26, 2024, ver. 1. DOI: 10.48550/ARXIV.2409.18210

(18) Rahman, F. Y.; Chakraborty, S.; Deb, R.; Uddin, Md. J.; Bhattacharjee, D.; Alibrahim, K. A.; Alodhayb, A. N.; Hussain, S. A. Clay Induced Performance Enhancement of a Plant Extract-Based WORM and RRAM for Sustainable Data Storage and Neuromorphic Computing Applications. *ACS Appl. Electron. Mater.* **2024**, *6* (9), 6591−6607.

(19) Bose, S.; Sinha, A.; Ghosh, S. In Situ Growth of Copper Channels within CuCl and PVDF Composite for Durable WORM Device Formation. *arXiv*, July 30, 2024, ver. 1. DOI: 10.48550/ARXIV.2407.20687

(20) Kim, H.; Hyun, D.; Hilal, M.; Cai, Z.; Moon, C. W. 2D and Quasi-2D Halide Perovskite-Based Resistive Switching Memory Systems. *Electronics* **2024**, *13* (17), 3572.

(21) Betal, A.; Bera, J.; Sharma, A.; Rath, A. K.; Sahu, S. Composition and Surface Morphology Invariant High On−Off Ratio from an Organic Memristor. *ACS Appl. Electron. Mater.* **2022**, *4* (3), 1109−1116.

(22) Wang, X.; Ali, N.; Bi, G.; He, L. High-Quality Organic−Inorganic Lead-Free Bismuth Halide Perovskite Film for Resistive Switching Memory Application. *J. Mater. Sci: Mater. Electron* **2024**, *35* (14), 971.

(23) Harshini, D.; Angela, V. M.; Devibala, P.; Imran, P. M.; Bhuvanesh, N. S. P.; Nagarajan, S. Improved Resistive Switching WORM Memory Behavior in D-π-A Architectures by Modifying the Terminal Donor Units. *ACS Appl. Electron. Mater.* **2022**, *4* (9), 4383−4395.

(24) Cheng, X.; Qin, Z.; Guo, H.; Dou, Z.; Lian, H.; Fan, J.; Qu, Y.; Dong, Q. Metallopolymeric Memristor Based Artificial Optoelectronic Synapse for Neuromorphic Computing. *ACS Appl. Electron. Mater.* **2024**, *6* (6), 4345−4355.

(25) Li, Y.; Qian, Q.; Zhu, X.; Li, Y.; Zhang, M.; Li, J.; Ma, C.; Li, H.; Lu, J.; Zhang, Q. Recent Advances in Organic-based Materials for Resistive Memory Applications. *InfoMat* **2020**, *2* (6), 995−1033.

(26) Rahman, F. Y.; Deb, R.; Sarkar, S.; Banik, H.; Uddin, Md. J.; Chakraborty, S.; Bhattacharjee, D.; Hussain, S. A. Resistive Switching Behavior Employing the *Ipomoea Carnea* Plant for Biodegradable Rewritable Read-Only Memory Applications. *ACS Appl. Electron. Mater.* **2023**, *5* (7), 3685−3697.

(27) Li, Z.; Hong, E. Y.-H.; Poon, C.-T.; Cheng, Y.-H.; Chan, M. H.-Y.; Leung, M.-Y.; Wu, L.; Yam, V. W.-W. Synthesis, Characterization, Supramolecular Self-Assembly, and Organic Resistive Memory Applications of BODIPY Derivatives. *ACS Materials Lett.* **2023**, *5* (3), 909−919.

(28) Gayathri, R.; Angela, V. M.; Devibala, P.; Imran, P. M.; Nagarajan, S. Tailoring the Resistive Switching WORM Memory Behavior of Functionalized Bis(Triphenylamine). *ACS Appl. Mater. Interfaces* **2023**, *15* (19), 23546−23556.

(29) Banik, H.; Sarkar, S.; Bhattacharjee, D.; Hussain, S. A. Transient WORM Memory Device Using Biocompatible Protamine Sulfate with Very High Data Retention and Stability. *ACS Appl. Electron. Mater.* **2021**, *3* (12), 5248−5256.

(30) Zhang, H.; Zhao, X.; Bai, J.; Hou, Y.; Wang, S.; Wang, C.; Ma, D. Ternary Memory Devices Based on Bipolar Copolymers with Naphthalene Benzimidazole Acceptors and Fluorene/Carbazole Donors. *Macromolecules* **2019**, *52* (23), 9364−9375.

(31) Yun, J.; Kim, D. Unraveling the Role of Polydopamines in Resistive Switching in Al/Polydopamine/Al Structure for Organic Resistive Random-Access Memory. *Polymers* **2022**, *14* (15), 2995.

(32) Shen, J.; Xue, F.; Wang, G.; Li, Y.; Dong, H.; Zhang, Q. Effective Transport Tunnels Achieved by 1,2,4,5-Tetrazine-Induced Intermolecular C−H···N Interaction and Anion Radicals for Stable ReRAM Performance. *ACS Appl. Mater. Interfaces* **2022**, *14* (6), 8218−8225.

(33) Kumar, A.; Baccoli, R.; Fais, A.; Cincotti, A.; Pilia, L.; Gatto, G. Substitution Effects on the Optoelectronic Properties of Coumarin Derivatives. *Applied Sciences* **2020**, *10* (1), 144.

(34) Jameel, E.; Umar, T.; Kumar, J.; Hoda, N. Coumarin: A Privileged Scaffold for the Design and Development of Antineurodegenerative Agents. *Chem. Biol. Drug Des* **2016**, *87* (1), 21−38.

(35) Deb, R.; De, U. C.; Bhattacharjee, D.; Hussain, S. A. Coumarin Based Non-Volatile WORM Device on a Graphite Coated Paper Substrate. *Interactions* **2024**, *245* (1), 267.

(36) *Vogel's Textbook of Practical Organic Chemistry*, 5th ed., 3rd impression.; Vogel, A. I., Furniss, B. S., Eds.; Pearson Education: New Delhi, 2007.

(37) Ocaya, R. O.; Al-Ghamdi, A.; Mensah-Darkwa, K.; Gupta, R. K.; Farooq, W.; Yakuphanoglu, F. Organic Photodetector with Coumarin-Adjustable Photocurrent. *Synth. Met.* **2016**, *213*, 65−72.

(38) Xiao, H.; Wang, Y.; Zhao, Y.; Zhang, R.; Kang, K.; Feng, Y.; Gao, Y.; Guo, H.; Lu, B.; Du, P.; Lu, X. Insight into the Charge Transfer Behavior of an Electrochemiluminescence Sensor Based on Porphyrin−Coumarin Derivatives with a Donor−Acceptor Configuration. *Chem. Sci.* **2024**, *15* (40), 16681−16687.

(39) Lin, S.; Chan, L.; Lee, R.; Yen, M.; Kuo, W.; Chen, C.; Jeng, R. Highly Efficient Carbazole- π -Dimesitylborane Bipolar Fluorophores for Nondoped Blue Organic Light-Emitting Diodes. *Adv. Mater.* **2008**, *20* (20), 3947−3952.

(40) Merlo, A. A.; Tavares, A.; Khan, S.; Leite Santos, M. J.; Teixeira, S. R. Liquid-Crystalline Coumarin Derivatives: Contribution to the Tailoring of Metal-Free Sensitizers for Solar Cells. *Liq. Cryst.* **2018**, *45* (2), 310−322.

(41) Rudra Paul, A.; Dey, B.; Suklabaidya, S.; Hussain, S. A.; Majumdar, S. 7-Alkoxy-Appended Coumarin Derivatives: Synthesis, Photo-Physical Properties, Aggregation Behaviours and Current−Voltage ($I - V$) Characteristic Studies on Thin Films. *RSC Adv.* **2021**, *11* (17), 10212−10223.

(42) Liu, Y.; Song, X.; He, J.; Zheng, X.; Wu, H. Synthetic Derivatives of Chrysin and Their Biological Activities. *Med. Chem. Res.* **2014**, *23* (2), 555−563.

(43) Ho, H. H. D.; Nguyen, N. H.; Nguyen, N. B.; Le, V. K.; Nguyen, N.-U. T.; Le Hoang Doan, T.; Nguyen, L. H. T.; Nguyen, T. H.; Pham, N. K. Development of Switching Memory Devices of Cellulose Fibers from Lotus Petioles. *J. Mater. Sci: Mater. Electron* **2024**, *35* (6), 387.

(44) Mehonic, A.; Cueff, S.; Wojdak, M.; Hudziak, S.; Jambois, O.; Labbé, C.; Garrido, B.; Rizk, R.; Kenyon, A. J. Resistive Switching in Silicon Suboxide Films. *J. Appl. Phys.* **2012**, *111* (7), No. 074507.

(45) Dehingia, A.; Ota, S.; Deb, R.; Das, U.; Roy, A. Effect of RF-Sputtering Temperature of ITO Electrodes on the Resistive Switching Behaviour of ITO/RbPbI$_3$ /Cu Devices. *Phys. Scr.* **2023**, *98* (11), No. 115917.

(46) Roldán, J. B.; Miranda, E.; Maldonado, D.; Mikhaylov, A. N.; Agudov, N. V.; Dubkov, A. A.; Koryazhkina, M. N.; González, M. B.; Villena, M. A.; Poblador, S.; Saludes-Tapia, M.; Picos, R.; Jiménez-Molinos, F.; Stavrinides, S. G.; Salvador, E.; Alonso, F. J.; Campabadal, F.; Spagnolo, B.; Lanza, M.; Chua, L. O. Variability in Resistive Memories. *Advanced Intelligent Systems* **2023**, *5* (6), No. 2200338.

(47) Yao, C.; Wu, C.; Gong, L.; Wu, Q.; Tian, T. Coexistence of Digital and Analog Resistive Switching Behaviors in Nanocrystalline Yttrium-Iron-Garnet Thin Films Achieved by Electrode Engineering. *Appl. Surf. Sci.* **2025**, *680*, No. 161329.

(48) Manoj Kumar, B.; Malavika, C.; Kannan, E. S. Defect-Engineered Resistive Switching in van Der Waal Metals. *IEEE Trans. Electron Devices* **2024**, *71* (11), 7144−7148.

(49) Kim, G.; Park, S.; Kim, S. Quantum Dots for Resistive Switching Memory and Artificial Synapse. *Nanomaterials* **2024**, *14* (19), 1575.

(50) Ahmad, I.; Lee, D.; Chae, M.; Kim, T.; Ali, M.; Kim, H.-D. Improved Resistive Switching Characteristics Observed in Amorphous Boron Nitride-Based RRAM Device via Oxygen Doping: A Study Based on Bulk and Interface Traps Analysis. *Materials Science in Semiconductor Processing* **2024**, *184*, No. 108805.

(51) Moazzeni, A.; Hamedi, S.; Kordrostami, Z. Switching Characteristic of Fabricated Nonvolatile Bipolar Resistive Switching Memory (ReRAM) Using PEDOT: PSS/GO. *Solid-State Electron.* **2022**, *188*, No. 108208.

(52) Wen, X.; Tang, W.; Lin, Z.; Peng, X.; Tang, Z.; Hou, L. Solution-Processed Small-Molecular Organic Memristor with a Very Low Resistive Switching Set Voltage of 0.38 V. *Appl. Phys. Lett.* **2023**, *122* (17), No. 173301.

(53) Song, Y.; Liu, J.; Li, W.; Liu, L.; Yang, L.; Lei, S.; Hu, W. Effect of Functional Groups on Microporous Polymer Based Resistance Switching Memory Devices. *Chem. Commun.* **2020**, *56* (47), 6356−6359.

(54) Ruan, L.; Tong, J.; Luo, F.; Wu, Y.; Qin, G.; Zhang, X. Discrete Resistive Switching Characteristics in Metal-Free Phthalocyanine and Dy-Phthalocyanine Based Devices. *Materials Today Communications* **2022**, *30*, No. 103131.

(55) Li, P.; Chan, C.-Y.; Lai, S.-L.; Chan, H.; Leung, M.-Y.; Hong, E. Y.-H.; Li, J.; Wu, H.; Chan, M.-Y.; Yam, V. W.-W. Three-Dimensional Spirothienoquinoline-Based Small Molecules for Organic Photovoltaic and Organic Resistive Memory Applications. *ACS Appl. Mater. Interfaces* **2020**, *12* (10), 11865−11875.

(56) Li, Y.; Zhu, X.; Li, Y.; Zhang, M.; Ma, C.; Li, H.; Lu, J.; Zhang, Q. Highly Robust Organometallic Small-Molecule-Based Nonvolatile Resistive Memory Controlled by a Redox-Gated Switching Mechanism. *ACS Appl. Mater. Interfaces* **2019**, *11* (43), 40332−40338.

(57) Gayathri, R.; Angela, V. M.; Devibala, P.; Imran, P. M.; Nagarajan, S. Tailoring the Resistive Switching WORM Memory Behavior of Functionalized Bis(Triphenylamine). *ACS Appl. Mater. Interfaces* **2023**, *15* (19), 23546−23556.

(58) Angela, V. M.; Harshini, D.; Anjali, A.; Imran, P. M.; Bhuvanesh, N. S. P.; Nagarajan, S. Enhancing the Resistive Switching Behavior of WORM Memory Devices Using D−π−A Based Ester-Flanked Quinolines**. *Chem.—Eur. J.* **2023**, *29* (8), No. e202202569.

(59) Bhagyanath, P. K.; Angela, V. M.; Asit, H.; Imran, P. M.; Bhuvanesh, N. S. P.; Nagarajan, S. Switching from Binary to Ternary WORM Memory Behavior of Benzothiadiazole-Based D−A System. *Mater. Adv.* **2024**, *5* (8), 3323−3333.

(60) Sd, A.; Battula, H.; Boppidi, P. K. R.; Kundu, S.; Chakraborty, C.; Jayanty, S. Photophysical, Electrochemical and Flexible Organic Resistive Switching Memory Device Application of a Small Molecule: 7,7-Bis(Hydroxyethylpiperazino) Dicyanoquinodimethane. *Org. Electron.* **2020**, *76*, No. 105457.

(61) Hwang, B.; Lee, J.-S. Hybrid Organic-Inorganic Perovskite Memory with Long-Term Stability in Air. *Sci. Rep* **2017**, *7* (1), 673.

(62) Liu, Z.; He, J.; Li, H.; Xu, Q.; Li, N.; Chen, D.; Wang, L.; Chen, X.; Zhang, K.; Lu, J. Organic Multilevel Memory Devices of Long-Term Environmental Stability via Incorporation of Fluorine. *Adv. Elect Materials* **2016**, *2* (5), No. 1500474.

(63) Zhang, Y.; Wu, H.; Bai, Y.; Chen, A.; Yu, Z.; Zhang, J.; Qian, H. Study of Conduction and Switching Mechanisms in Al/AlOx/WOx/W Resistive Switching Memory for Multilevel Applications. *Appl. Phys. Lett.* **2013**, *102* (23), No. 233502.

(64) Lim, E.; Ismail, R. Conduction Mechanism of Valence Change Resistive Switching Memory: A Survey. *Electronics* **2015**, *4* (3), 586−613.

(65) Wang, C.; Wu, H.; Gao, B.; Zhang, T.; Yang, Y.; Qian, H. Conduction Mechanisms, Dynamics and Stability in ReRAMs. *Microelectron. Eng.* **2018**, *187−188*, 121−133.

(66) Das, U.; Dehingia, A.; Paul, B.; Sarkar, P. K.; Roy, A. Improvement of the Resistive Switching Characteristics upon Halide Mixing in an All-Inorganic $RbPbI_3$ Perovskite Polymer Composite Based Flexible Device. *J. Phys. Chem. C* **2021**, *125* (24), 13610−13618.

(67) Das, U.; Das, D.; Paul, B.; Rabha, T.; Pattanayak, S.; Kanjilal, A.; Bhattacharjee, S.; Sarkar, P.; Roy, A. Induced Vacancy-Assisted Filamentary Resistive Switching Device Based on $RbPbI_{3-x}$ Cl_x Perovskite for RRAM Application. *ACS Appl. Mater. Interfaces* **2020**, *12* (37), 41718−41727.

(68) Hosseini, N. R.; Lee, J. Biocompatible and Flexible Chitosan-Based Resistive Switching Memory with Magnesium Electrodes. *Adv. Funct Materials* **2015**, *25* (35), 5586−5592.

(69) Jeong, H. Y.; Lee, J. Y.; Ryu, M.; Choi, S. Bipolar Resistive Switching in Amorphous Titanium Oxide Thin Film. *Physica Rapid Research Ltrs* **2010**, *4* (1−2), 28−30.

(70) Xue, J.; Yang, D.; Wang, J.; Wang, H.; Dai, Y.; Wang, S.; Lei, X.; Yan, J.; Zhao, W. Conduction Mechanisms Analysis of ZrO2-Based Electrochemical Metallization RRAM in Different RESET Modes. *Chinese Journal of Physics* **2024**, *91*, 369−376.

(71) Sun, Y.; Li, L.; Wen, D.; Bai, X.; Li, G. Bistable Electrical Switching and Nonvolatile Memory Effect in Carbon Nanotube−Poly(3,4-Ethylenedioxythiophene):Poly(Styrenesulfonate) Composite Films. *Phys. Chem. Chem. Phys.* **2015**, *17* (26), 17150−17158.

(72) Kushwaha, P. K.; Srivastava, S. K. Tuning Optoelectronic Properties of Indandione-Based D-A Materials by Malononitrile Group Acceptors: A DFT and TD-DFT Approach. *J. Mol. Model* **2024**, *30* (10), 356.

(73) Tong, J.; An, L.; Yang, K.; Liang, Z.; Yu, T. *A-A′-A Structured Methoxy-Modified Perylenediimide Dimeric Acceptors at the Outside-Bay Position: Synthesis, Spectroscopic Property and Photovoltaic Application*. SSRN 2024. DOI: 10.2139/ssrn.4941020.

(74) Shen, H.; Li, Y.; Li, Y. Self-assembly and Tunable Optical Properties of Intramolecular Charge Transfer Molecules. *Aggregate* **2020**, *1* (1), 57−68.

(75) Park, Y. I.; Kuo, C.-Y.; Martinez, J. S.; Park, Y.-S.; Postupna, O.; Zhugayevych, A.; Kim, S.; Park, J.; Tretiak, S.; Wang, H.-L. Tailored Electronic Structure and Optical Properties of Conjugated Systems through Aggregates and Dipole−Dipole Interactions. *ACS Appl. Mater. Interfaces* **2013**, *5* (11), 4685−4695.

(76) Elgrishi, N.; Rountree, K. J.; McCarthy, B. D.; Rountree, E. S.; Eisenhart, T. T.; Dempsey, J. L. A Practical Beginner's Guide to Cyclic Voltammetry. *J. Chem. Educ.* **2018**, *95* (2), 197−206.

(77) Hou, J.; Zhang, B.; Li, D.; Fu, Y.; Liu, G.; Chen, Y. Enabling Superior Stretchable Resistive Switching Memory *via* Polymer-Functionalized Graphene Oxide Nanosheets. *J. Mater. Chem. C* **2019**, *7* (46), 14664−14671.

(78) Riemann, A.; Rankin, L.; Henry, D. Atomic Charge Dependency of Spiropyran/Merocyanine Adsorption as a Precursor to Surface Isomerization Reactions. *ACS Omega* **2024**, *9* (1), 798−810.

(79) Xu, J.; Wen, L.; Zhou, W.; Lv, J.; Guo, Y.; Zhu, M.; Liu, H.; Li, Y.; Jiang, L. Asymmetric and Symmetric Dipole−Dipole Interactions Drive Distinct Aggregation and Emission Behavior of Intramolecular Charge-Transfer Molecules. *J. Phys. Chem. C* **2009**, *113* (15), 5924−5932.

(80) Luo, Y.; Xue, Z.; Li, Y.; Liu, H.; Yang, W.; Li, Y. Controllable Growth of Organic Nanostructures from 0D to 1D with Different Optical Properties. *RSC Adv.* **2015**, *5* (122), 100457−100463.